Catal Surv Asia (2016) 20:141–166
DOI 10.1007/s10563-016-9216-8

Recent Advances in the Preferential Thermal-/Photo-Oxidation of Carbon Monoxide: Noble Versus Inexpensive Metals and Their Reaction Mechanisms

Yusuke Yoshida[1,2] · **Yasuo Izumi**[1]

Abstract Preferential oxidation (PROX) of CO is applicable because of its low cost, ease of implementation, and low loss of H_2 during purification. Mo–SiO_2 and Cr–SiO_2 photocatalysts utilized charge separation at metal=O bonds, and the PROX selectivity of CO was high. The CO PROX rates using semiconductor-based photocatalysts were comparable to those of photocatalysts (380 μmol h^{-1} g_{cat}^{-1}) and were also selective (100 %). These photocatalysts are advantageous because they do not activate H_2 in comparison to noble metal catalysts. Below 473 K using noble metals, Ru, Rh, Pt, or Au supported on reducible metal oxides exhibited excellent CO thermal-PROX rates of ~4900 μmol h^{-1} g_{cat}^{-1}; however, the CO PROX selectivity of ~48 % was insufficient because of H_2 activation on noble metals in nature. CO adsorbed onto TiO_2 and O_2 was stabilized at the interface between a Ti site and an Au atom. Weakly adsorbed water increased the effective number of active sites by stabilizing Au–OOH or Au–COOH. The PROX rates of CO using Au/TiO_2-based catalysts under dark conditions increased under UV–visible light by the effect of charge separation and surface plasmon resonance and the promoted electron transfer to the adsorbed O_2. In the case of CuO–CeO_2 catalysts, CO adsorbed onto CuO and reacted with lattice O atoms at the boundary between CuO and CeO_2 to form CO_2 at an O vacancy, which was subsequently filled with an O_2 molecule. The combination of Cu or Co with a reducible metal oxides also provided performance comparable to or higher than that of CuO–CeO_2 owing to adequate standard reduction potential for Cu^{2+}, Co^{3+}, $Mn^{3+/4+}$, and Ce^{4+}. Finally, binary metal–organic framework consisting of oxyhydroxide Ti clusters interlinked by organic ligands and Cu oxyhydroxide ligands showed superior CO PROX performance (76 % conversion and 99 % selectivity) to that achieved using CuO–CeO_2 owing to effective dispersion of Cu–O–Ti connection in microporous crystallites. Further progress is needed to alleviate the activity loss in the presence of moisture and/or CO_2 based on suggestions that steric hindrance of some types of microporous crystallites would suppress the blocking of moisture or CO_2.

Graphical Abstract

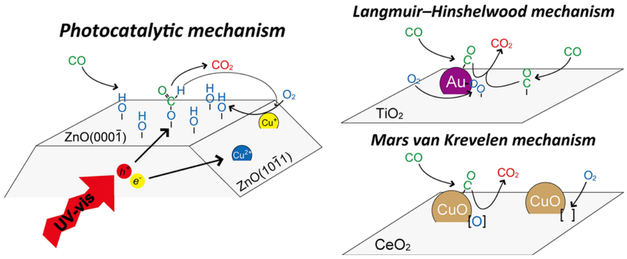

Keywords Preferential CO oxidation of CO · Photo PROX · Copper catalyst · Cobalt catalyst · Binary metal–organic framework

1 Introduction

The production, storage, and transport of H_2 are key technologies for the emergence of a H_2 energy society in the near future [1]. Fuel cells (FCs) are the key device for

---

✉ Yasuo Izumi
yizumi@faculty.chiba-u.jp

[1] Department of Chemistry, Graduate School of Science, Chiba University, Yayoi 1-33, Inage-ku, Chiba 263-8522, Japan

[2] Present Address: Innovation Research Center of Fuel Cells, The University of Electro-Communications, 1-5-1 Chofugaoka, Chofu, Tokyo 182-8585, Japan

converting H_2 into electricity for use in vehicles, mobile phones, and residences and will be indispensable in a H_2 energy society [2]. H_2 production from water utilizing sustainable energy is ideal; however, these methods are expensive, and a practical H_2 source continues to be fossil fuels [3]. A substantial part of the cost of FCs can be attributed to the electrode catalysts, which are mostly composed of Pt. Currently, most H_2 is produced via the reforming of fossil fuels, and a few percent of CO inevitably remains because of the equilibrium limitation of the water–gas shift reaction (WGSR):

$$H_2O + CO \rightleftarrows H_2 + CO_2. \tag{1}$$

Here, electrode catalysts are easily deactivated if more than 10 parts per million (ppm), i.e., more than 1.0 Pa of ambient pressure, of CO is contained as an impurity in H_2 because of the strong irreversible adsorption of CO onto the Pt surface [4].

Well-known techniques for purifying H_2 include pressure swing adsorption (PSA) [5], separation using metal membranes [6], cryogenic separation [6], preferential oxidation (PROX) of CO [7–11], and methanation of CO [9]. PSA and metal membrane separation are advantageous for achieving higher H_2 purity, whereas cryogenic separation recovers a larger amount of H_2. The PSA apparatus incurs high initial investment costs and is therefore not appropriate for small-scale or personal use. PROX is potentially applicable since it has the lowest cost and easiest implementation of the aforementioned methods, without the associated loss of H_2 during purification. Membrane separation typically uses Pd metal, whereas the PROX reaction of CO often utilizes expensive metals such as Au and Pt as the supported nanoparticle metal. The methanation of CO using catalysts generally requires reaction temperatures greater than 573 K. Thus, to generate environmentally benign energy for small-scale or personal use, a new method for the purification of H_2 that employs a cost-effective and sustainable membrane/catalyst is strongly demanded.

PROX catalysts based on noble metals [8–10] and transition/rare-earth metals [9, 11] were reviewed in 2008–2014; however, inexpensive PROX photocatalysts assuming solar light utilization have never been reviewed; in addition, recently developed, inexpensive, and highly efficient Cu, Ni, and Co PROX catalysts need to be reviewed based on their efficiencies and plausible reaction mechanisms using state-of-the-art surface analytic techniques. This review covers findings related to both photocatalysts and thermal catalysts and the understanding of their mechanisms to examine the major fundamental research trends of PROX catalysis applicable for an H_2 society. Because it is practically desirable to conduct PROX reactions between the temperatures associated with low-temperature WGSRs (473–523 K) and the operation of polymer electrolyte (PE) FCs (353–373 K), this review focuses on photo-PROX and photoassisted- or thermal-PROX reactions in the temperature range from 353 to 523 K.

Various authors have noted that photocatalytic rates are not always proportional to the amount of photocatalyst charged as a suspension in a reaction solution [12] or as a film in contact with the reaction gas [3, 13]; however, the photo-PROX rates of CO using Cu–ZnO as fine powder were well proportional to the amount of Cu–ZnO charged as a fine powder in contact with the reaction gas (Fig. 1) [14]. Direct comparison between the photocatalytic and thermal PROX rates of CO is difficult. Nonetheless, we herein introduce catalysts as fine powders or molded and fractioned powders by mesh and express the rates in units of

$$\frac{\text{Amount of products}}{\text{Reaction duration time} \times \text{Amount of catalyst}} \left(\mathrm{mol\,h^{-1}\,g_{cat}^{-1}}\right) \tag{2}$$

to survey the major trends related to the photo/thermal-PROX of CO.

2 Photocatalytic PROX Reactions of CO

2.1 Photocatalytic Water–Gas Shift Reaction

The WGSR (Eq. 1) involves neither the PROX reaction nor the oxidation reaction of CO and apparently seems beyond

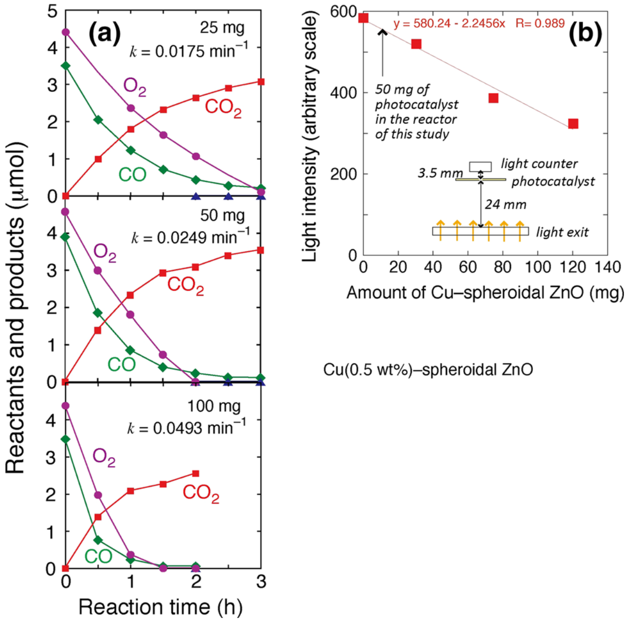

Fig. 1 **a** Dependence of time course of PROX reaction of CO in H_2 on amount of Cu–spheroidal ZnO used (25–100 mg) under illumination with UV–visible light. **b** Dependence of transmitted UV–visible light intensity through 30–120 mg of Cu–spheroidal ZnO in 5.3 cm^2 area. Distance between bottom of reactor and lamp exit was set to 24 mm [14]. Copyright (2012) Elsevier

the scope of this review; however, the oxidation of CO by O and/or OH groups photo-decomposed from water was proposed in 1980 [15]. Under 3.2 kPa of water, H_2 was formed; however, the H_2 formation rate was gradually decreased using Pt(2 wt%)/TiO_2 irradiated with a 200 W high-pressure Hg lamp that was filtered through $NiSO_4$ solution. Conversely, 80 Pa of ^{13}CO and 3.2 kPa of water were reacted using Pt/TiO_2 at 273–298 K irradiated by the same light source. The H_2 formation rate became constant and essentially remained unchanged with decreasing rate of CO, demonstrating that CO picked up O species derived from water, thereby maintaining a clean surface. Based on the band energy level of n-type TiO_2 and Pt nanoparticles connected by a Schottky barrier to trap electrons in Pt nanoparticles, the following reaction steps were proposed:

$$TiO_2 + h\nu \rightarrow h^+ + e^-, \quad (3)$$

$$h^+(TiO_2) + H_2O \rightarrow \cdot OH + H^+, \quad (4)$$

$$CO + \cdot OH \rightarrow CO_2 + H, \quad (5)$$

$$e^-(Pt) + H^+ \rightarrow \cdot H, \quad (6)$$

and

$$2 \cdot H \rightarrow H_2. \quad (7)$$

2.2 Photocatalytic Oxidation Using Metal Oxide-Based Catalysts

Before we discuss photocatalytic PROX reactions of CO, we briefly introduce pioneering and recent works related to photocatalytic simple oxidations of CO as the basis to understand the photocatalytic PROX reaction mechanisms.

2.2.1 TiO_2 Catalysts

The feasibility of photocatalytic CO oxidation using TiO_2 and the proposed reaction mechanism was reported in 1996 [16]. Surface O vacancy sites were formed by annealing rutile-type TiO_2(110) crystal at temperatures greater than 400 K. Molecular O_2 chemisorbed at O vacancy sites on TiO_2(110) at 105 K (Fig. 2) mainly desorbed as O_2 and partially oxidized coadsorbed CO molecules to produce CO_2 when irradiated by light with an energy greater than 3.1 eV. The decay times for CO_2 formation and O_2 desorption steps from relatively stable adsorbed O_2 species were essentially identical, suggesting common chemisorbed O_2 species desorbed or oxidized CO molecules. Because no CO_2 desorption was monitored in the absence of light [16], photoproduction of CO_2 should be enabled energetically via the hole oxidation of CO (Eq. 8) and electron reduction of O_2-derived species (Eq. 9).

$$h^+(TiO_2) + CO \rightarrow CO^+, \quad (8)$$

$$e^-(TiO_2) + O_2 \rightarrow O^- + O\,(\text{vacancy filled}), \quad (9)$$

and

$$CO^+ + O^- \rightarrow CO_2. \quad (10)$$

2.2.2 PdPt/TiO_2 Catalysts

Photooxidation of CO was recently reported using bimetallic PdPt nanoparticles (mean size 1–2 nm) formed on TiO_2 [17]; the authors discussed the effects of humidity. The poisoning by moisture is one of the most serious problems for PROX catalysts of CO. When 3.7 kPa of moisture was added at 313 K, the CO conversion using 0.3 wt% of Pt over TiO_2 and Pd(0.3 wt%)/TiO_2 decreased by factors of 0.65–0.40 times: from 79 to 51 % and from 84 to 34 %, respectively (Tables 1a, c, 2a, c). By contrast, the CO conversion using bimetallic $Pd_{0.5}Pt_{0.5}$(in total 0.3 wt%)/TiO_2 was higher as a consequence of the bimetallic effect in the absence of moisture (95 %) and remained high at 90 % in the presence of 3.7 kPa of moisture (Tables 1b, 2b). The "bimetallic effect" enabled to design neighboring sites for CO and O_2 adsorption.

Partial segregation of Pd to the corners, edges, and faces was suggested based on simulated high-angle annular dark field (HAADF) scanning transmission electron microscopy (STEM) images for $Pd_{0.2}Pt_{0.8}$ nanoparticles (Fig. 3). However, a more random distribution of Pd and Pt was suggested for $Pd_{0.5}Pt_{0.5}$ nanoparticles based on the limited population of surface sites of higher surface energies, the fact that the samples were prepared at room temperature

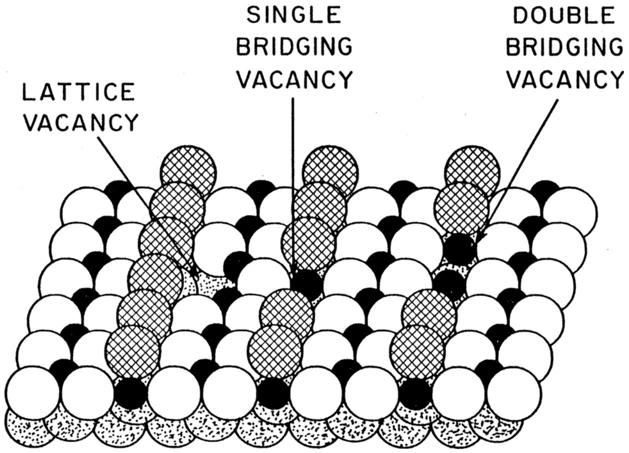

Fig. 2 Rutile-type TiO_2(110) surface illustrating O vacancy sites produced by annealing: (*cross-hatched symbols*) bridging O^{2-} overlayer ions, (*open symbols*) in-plane O^{2-} ions, (*solid symbols*) Ti^{4+} or Ti^{3+} ions, and (*shaded symbols*) bulk O^{2-} ions [16]. Copyright (1996) American Chemical Society

Table 1 Comparison of rates of photocatalytic PROX or oxidation reactions of CO reported in literature

Entry	Catalyst		*T* (K)	Light	System	Reactants *P*	$R_{CO \to CO2}$ (μmol h^{-1} g_{cat}^{-1})[1]	CO Conv. (%)[2]	CO_2 Selec. (%)[3]	Ref.
	Type	*W* (mg)								
a[4]	Pt (0.3 %)/TiO_2	100	313	8 W Black light	Flow (250 mL min^{-1})	CO 25 Pa, O_2 21.2 kPa	1200	79		[17]
b[4]	$Pd_{0.5}Pt_{0.5}$(0.3 %)/TiO_2						1400	95		
c[4]	Pd (0.3 %)/TiO_2						1300	84		
d	NiO(0.5 %)–TiO_2	50	293	100 W HP Hg, H_2O filter	Closed circulation	CO 92 Pa, O_2 180 Pa, H_2 590 Pa	38	89 @3 h	98 @3 h	[27]
e	Mo(0.6 %)–SiO_2						95	~100 @3 h	99 @3 h	[19]
f	Mo(1.0 %)-MCM-41	20					62	98 @3 h	98	[24]
g	Cr(0.7 %)-MCM-41			500 W Xe ($\lambda > 420$ nm)			380	~100 @2.5 h	97	[25]
h	Cu(0.5 %)-spheroidal ZnO	50	<313	500 W Xe arc		CO 64 Pa, O_2 150 Pa, H_2 6.4 kPa	84	100 @3 h	94	[14]
i						CO 64 Pa, O_2 76 Pa, H_2 6.4 kPa	56	91 @3 h	99	
j	Cu(0.5 %)-disk-like ZnO						59	91 @3 h	99	[28]
k	Cu(0.1 %)-spheroidal ZnO						97	97 @3 h	96	
l	Cu(0.5 %)-spheroidal ZnO						82	97 @3 h	99	
m	Cu(0.32 %)-rod-like ZnO						16	30 @3 h	100	

W sample weight charged, *T* reaction temperature, *P* pressure

[1] $R_{CO \to CO_2}$: CO removal rate

[2] CO Conv.: CO conversion (%) = $100 \times (n_{CO,Start} - n_{CO,End})/n_{CO,Start}$

[3] CO_2 Selec.: CO_2selectivity(%) = $100 \times n_{CO_2}/(n_{CO_2} + n_{H_2O})$

[4] Not PROX but simple oxidation

via liquid-phase reduction and were not calcined, and Fourier transform infrared spectroscopy results. The surface Pt sites were suggested to adsorb O_2 and water preferentially, leaving Pd sites free for CO adsorption.

In summary, supported PdPt photocatalysts facilitated CO oxidation at rates of 1200–1400 μmol h^{-1} g_{cat}^{-1}; these rates are similar to the photo-PROX rates obtained using supported Au catalysts if the inhibiting effects of predominant H_2 gas are neglected in the Au-catalyzed photo-PROX of CO. Importantly, this study provides a solution for one of the most serious problems for PROX: deactivation by humidity. Neighboring sites to CO adsorption sites to preferentially adsorb water and thus to liberate CO adsorption sites are required.

2.3 Photocatalytic PROX Using Inexpensive Elements Supported on Metal Oxides

For H_2 purification, the PROX reaction of CO using catalysts that do not contain noble metals and that can be excited under natural light is ideal. In this category, two types of photocatalysts have been reported. One is metal complex-like photocatalysts supported on metal oxides, in which charge separation occurs at the chemical bonds of molecule-like moieties upon irradiation. The other type is semiconductor photocatalysts, in which charge separation occurs in the bulk [18]. The advantage of photocatalytic PROX is selectivity toward CO PROX compared to H_2 oxidation by-reaction because complex-like or

Table 2 Comparison of effects of CO_2 and/or moisture in feed gas on PROX reactions of CO reported in literature

Entry	Catalyst	T (K)	Flow rate ($mL\ min^{-1}$)	CO Conv. (%)[1]				CO_2 Selec. (%)[2]				Ref.
				No addition	CO_2	Moisture	CO_2 + moisture	No addition	CO_2	Moisture	CO_2 + moisture	
a[3]	Pt(0.3 %)/TiO_2	313, 8 W Black light	250	79		51 (3.7 kPa H_2O)						17
b[3]	$Pd_{0.5}Pt_{0.5}$(0.3 %)/TiO_2			95		90 (3.7 kPa H_2O)						
c[3]	Pd(0.3 %)/TiO_2			84		34 (3.7 kPa H_2O)						
d	Pt/γ-Al_2O_3	373	100	5.0	3.3 (15 kPa CO_2)			49 @398 K	38 @398 K (15 kPa CO_2)			60
e	Au/α-Fe_2O_3			97	79 (15 kPa CO_2)			48	45 (15 kPa CO_2)			
f	CuO–CeO_2			63	23 (15 kPa CO_2)			~100	~100 (15 kPa CO_2)			
g	Pt/γ-Al_2O_3		21	20	17 (15 kPa CO_2)		42 (15 kPa CO_2 + 10 kPa H_2O)	44	50 (15 kPa CO_2)		42 (15 kPa CO_2 + 10 kPa H_2O)	
h	Au/α-Fe_2O_3			95 @353 K	97 @368 K (15 kPa CO_2)		99 (15 kPa CO_2 + 10 kPa H_2O)	39 @353 K	41 @368 K (15 kPa CO_2)		54 (15 kPa CO_2 + 10 kPa H_2O)	
i	CuO–CeO_2			96	59 (15 kPa CO_2)		11 @393 K (15 kPa CO_2 + 10 kPa H_2O)	~100	~100 (15 kPa CO_2)		~100 (15 kPa CO_2 + 10 kPa H_2O)	
j	Cu-Fe/$K_{2x+y}Mn^{II}_xMn^{III}_yMn^{IV}_{8-x-y}O_{16}$		100	27	16 (10 kPa CO_2)	14 (10 kPa H_2O)	10 (10 kPa CO_2 + 10 kPa H_2O)	91	91 (10 kPa CO_2)	~100 (10 kPa H_2O)	95 (10 kPa CO_2 + 10 kPa H_2O)	83
k	CuO(17 %)–ZnO(46 %)–TiO_2(37 %)	363	18 000 h^{-1}	32	10 (15 kPa CO2)			~100	~100			84
l	Co_3O_4(20 %)/$Ce_{0.85}Zr_{0.15}O_2$	373	250 $mL\ min^{-1}\ g^{-1}$	36	~0 (10 kPa CO_2)	4.3 (10 kPa H_2O)	2.4 (10 kPa CO_2 + 10 kPa H_2O)	~100	80 (10 kPa CO_2)	~100 (10 kPa H_2O)	~100 (10 kPa CO_2 + 10 kPa H_2O)	89
m	Mn(2.6 %)–Co(11 %)–CeO_2	448	2.1 mg mL^{-1} min	~100	95 (20 kPa CO_2)			49	55 (20 kPa CO_2)			90
n	Co(3.2 %)/$SrCO_3$	513	32	96	38 (20 kPa CO_2)		27 (18 kPa CO_2 + 10 kPa H_2O)	68	74 (20 kPa CO_2)		72 (18 kPa CO_2 + 10 kPa H_2O)	93

Table 2 continued

Entry	Catalyst	T (K)	Flow rate (mL min^{-1})	CO Conv. (%)[1]				CO_2 Selec. (%)[2]				Ref.
				No addition	CO_2	Moisture	CO_2 + moisture	No addition	CO_2	Moisture	CO_2 + moisture	
o	Co(3.2 %)–Bi(0.3 %)/$SrCO_3$						63 (18 kPa CO_2 + 10 kPa H_2O)				69 (18 kPa CO_2 + 10 kPa H_2O)	

T reaction temperature

[1] CO Conv.: CO conversion (%) = $100 \times (n_{CO,Start} - n_{CO,End})/n_{CO,Start}$

[2] CO_2 Selec.: CO_2selectivity(%) = $100 \times n_{CO_2}/(n_{CO_2} + n_{H_2O})$

[3] Not PROX but simple oxidation

semiconductor active sites basically activate polar molecules and does not activate H_2 compared to facile H_2 dissociative adsorption due to free electrons in metals and following reaction on metal surface for thermal PROX reaction.

2.3.1 *Charge Separation at Bonds*

As an example of a metal complex-like photocatalyst supported on SiO_2, a Mo–SiO_2 photocatalyst consisting of 0.6 wt% Mo (oxomolybdenum complex) performed well, with a CO conversion of ~100 % at 3 h and a CO_2 selectivity of 99 % under an initial reaction gas composition of CO (3.8 μmol) + O_2 (7.5 μmol) + H_2 (24.6 μmol) and illumination by a high-pressure Hg lamp. The Mo–SiO_2 photocatalyst reduced CO to less than 10 ppm in H_2, satisfying the requirement for the use of H_2 in PEFCs (Table 1e) [19]. Based on Mo K-edge extended X-ray absorption fine structure (EXAFS) curve-fit analysis [20], the predominant monomeric tetrahedral $(O{=})_2Mo(-O_{surface})_2$ species were proposed to be the active sites. Therefore, charge separation at chemical bonds is likely responsible for the photocatalysis. The charge-transfer triplet state at the Mo=O bond of $[Mo^{6+}{=}O^{2-}]$—specifically, $[Mo^{5+}{-}O^{-}]^{\ddagger}$ and/or a reduced state of Mo^{4+}—both induced by the irradiation of UV–visible light, were suggested to be responsible for CO PROX (Scheme 1).

The quenching rates of photoluminescence of Mo–SiO_2 were evaluated by the addition of CO, O_2, and H_2 to evaluate each reactivity on the photocatalyst [21]. The data were fitted to the Stern–Volmer equation [22, 23]:

$$\frac{\text{Yield of photoluminescence}}{\text{Yield of photoluminescence}_{\text{with quencher}}} = 1 + \tau_0 k_{\text{quench}}[\text{quencher}], \tag{11}$$

where τ_0 is the lifetime of the charge-transfer triplet excited state $[Mo^{5+}{-}O^{-}]^{\ddagger}$ in the absence of a quencher, and k_{quench} is the absolute quenching rate constant and thus a criterion of reactivity of CO, O_2, and H_2. The obtained k_{quench} values decreased in the order (Table 3)

$$CO > O_2 > H_2 \quad (\text{Table 3, Mo}{-}\text{SiO}_2), \tag{12}$$

demonstrating preferable interaction of CO with intermediate $[Mo^{5+}{-}O^{-}]^{\ddagger}$ species excited by light. Lowest interaction with H_2 means lowest rate of unfavorable side-reaction of CO PROX:

$$2H_2 + O_2 \rightarrow 2H_2O. \tag{13}$$

Mo–MCM-41 exhibited CO photo-PROX performance (Table 1f) similar to that of Mo–SiO_2, and the k_{quench} values decreased in the order

$$CO > O_2 \gg H_2 \quad (\text{Table 3, Mo} - \text{MCM-41}), \tag{14}$$

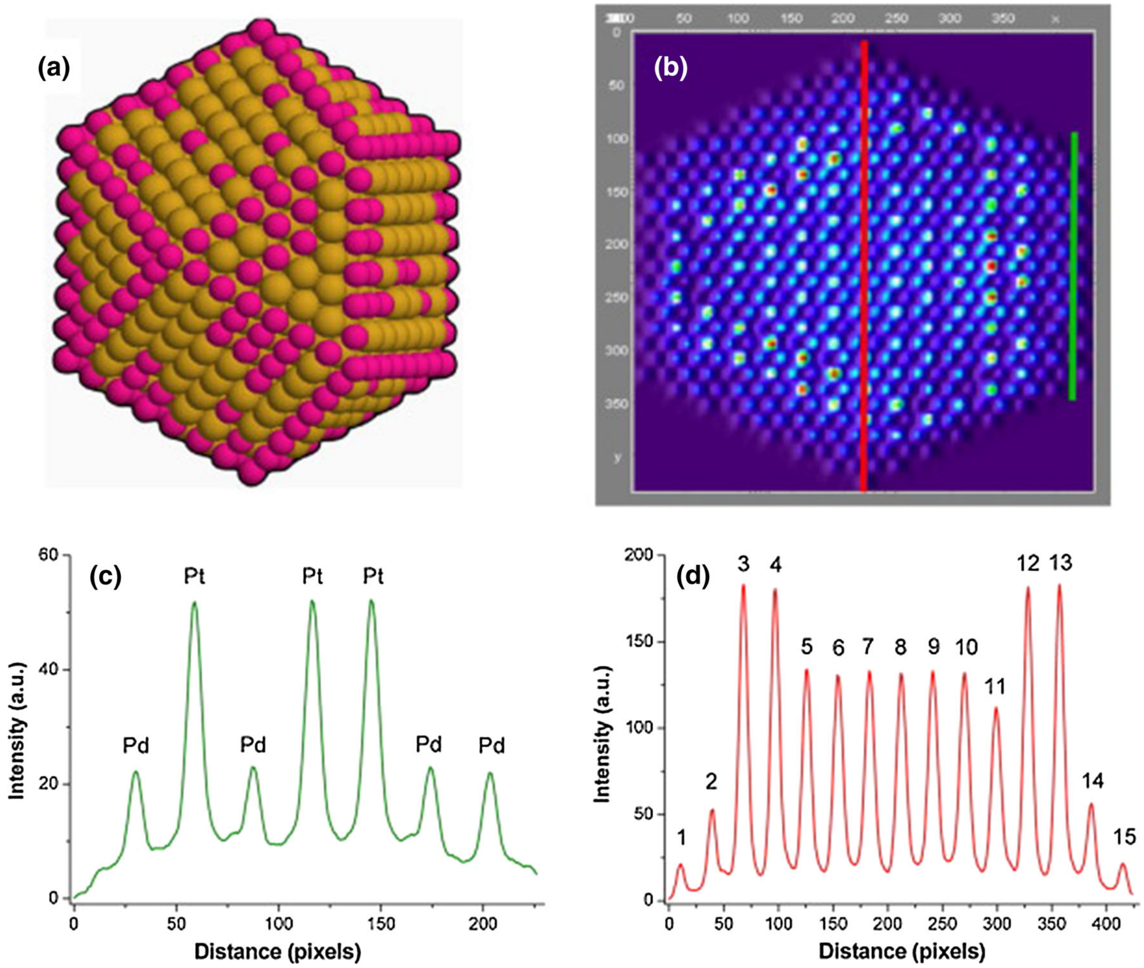

Fig. 3 Simulation of **a** 1406-atom cuboctahedral $Pd_{0.2}Pt_{0.8}$ nanoparticle with Pd (*red/darker spheres*) surface segregation versus Pt (*yellow/thinner spheres*); **b** HAADF-STEM image of cuboctahedron; HAADF-STEM intensity profiles at **c** border (*green/thinner line*) and **d** core (*red/darker line*) of cuboctahedron [17]. Copyright (2015) Elsevier (Color figure online)

Scheme 1 Photocatalytic reaction cycle in photocatalytic PROX of CO on tetrahedrally coordinated Mo^{6+}-oxide species [21]. Copyright (2007) Elsevier

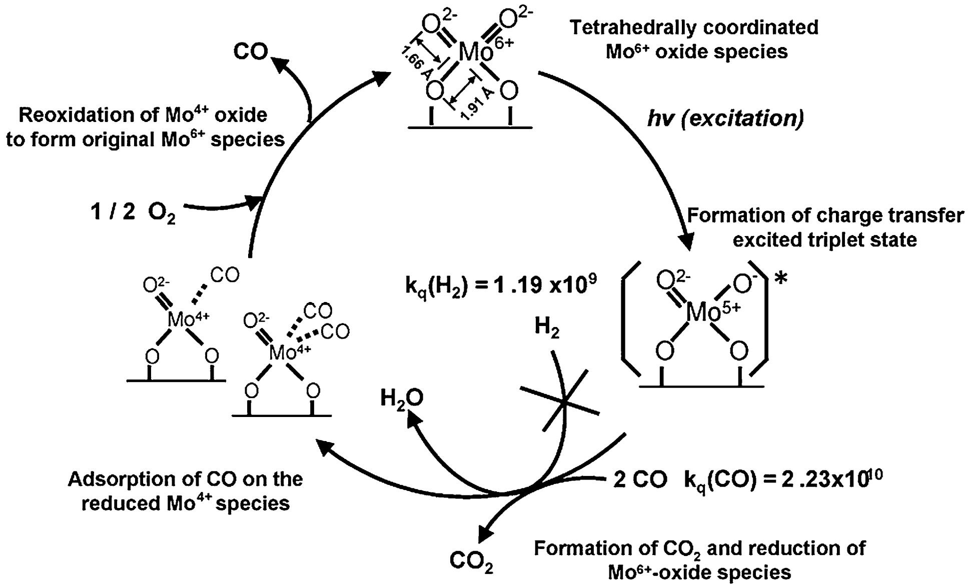

Table 3 Different rate constant k_{quench} values (mol^{-1} s^{-1}) for supported Mo and Cr photocatalysts depending on quenchers

Photocatalyst	Quencher			Ref.
	CO	O_2	H_2	
Mo–SiO_2	2.23×10^{10}	1.22×10^{10}	1.19×10^{9}	[21]
Mo–MCM-41	2.36×10^{10}	1.33×10^{10}	7.73×10^{8}	[24]
Cr–MCM-41	5.91×10^{9}	1.12×10^{10}	8.63×10^{5}	[25]

demonstrating a trend similar to that of Mo–SiO_2 that leads to preferable photo-PROX reaction of CO [24].

Under irradiation by visible light ($\lambda > 420$ nm), [Cr^{6+}=O^{2-}] species also exhibited charge transfer to an excited triplet [Cr^{5+}–O^{-}]‡ in the case of Cr–MCM-41 [25]. The CO PROX reaction rate (380 μmol h^{-1} g_{cat}^{-1}; Table 1) was superior to that achieved using Mo–MCM-41 (62 μmol h^{-1} g_{cat}^{-1}) by a factor of 6.1 under similar reaction conditions (Tables 1f, g). On the other hand, the absolute quenching rate constant k_{quench} values in Eq. 11 for photoluminescence decreased in the order

$$O_2 > CO \gg H_2 \quad (\text{Table 2, Cr} - \text{MCM-41}), \tag{15}$$

demonstrating preferential reactivity of [Cr^{5+}–O^{-}]‡ species with O_2 rather than H_2 and supporting better PROX performance of CO. This order differs from that observed for Mo catalysts, in which the values for CO were the greatest (Table 3). This difference suggests the relative importance of reductive O_2 activation compared to oxidative CO activation on the supported metal (Mo or Cr) complexes (Scheme 1). Importantly, the k_{quench} (H_2) value for Cr–MCM-41 was smaller by an order of 3–4 compared to those for Mo–MCM-41 and Mo–SiO_2 (Table 3). Weaker interaction of catalyst with predominate H_2 may lead to higher CO PROX reaction rates (Table 1). Furthermore, photocatalysis using isolated Ti-, V-, and Cr-oxides within zeolites has already been reviewed for CO PROX, CO_2 photoreduction, and NO decomposition reactions [26].

In summary, metal complex-like supported inexpensive Mo and Cr photocatalysts exhibited photo-PROX rates ranging from 62 to 380 μmol h^{-1} g_{cat}^{-1}. The rates were substantially lower than those achieved using expensive Au catalysts. By contrast, the CO PROX selectivity was consistently higher (97–99 %) than those achieved with Au-based catalysts due to the difference of polar metal complex and metal surface with free electrons.

2.3.2 *Charge Separation in Semiconductors*

Photo-PROX reactions of CO using semiconductors in the presence of a NiO/TiO_2 photocatalyst consisting of 0.5 wt% NiO have been reported to result in CO conversion of 89 % and CO_2 selectivity of 98 % at 3 h for a reaction-gas mixture composed of CO (3.8 μmol) + O_2 (7.5 μmol) + H_2 (24.6 μmol) irradiated by UV light (Table 1d) [27]. The oxidation of CO and reduction reactions should take place over TiO_2 and electron-trapping NiO nanoparticles, respectively, based on Sect. 2.1. Polar TiO_2 surface did not activate H_2 and the Ni sites oxidized rather than Ni^0 metal did not dissociate H_2, leading to high selectivity of CO PROX.

Detailed reaction mechanism recently reported for Cu–ZnO photocatalysts [14, 28]. The semiconductor properties of ZnO [14, 28] are similar to those of TiO_2 [29–34]. Spheroidal ZnO nanocatalysts with an average major axis of 47 nm and an average minor axis of 22 nm and combined with 0.5 wt% of adsorbed Cu^{2+} ions enabled 100 % CO conversion and 94 % CO_2 selectivity in 3 h under irradiation by UV–visible light (Table 1h). The performance was comparable to those using metal complex-like photocatalysts (see the Sect. 2.3.1) and the other semiconductor photocatalysts (this section). The rate corresponds to the preferential photooxidation of 9700 ppm of CO to 0.35 ppm in 6.3 kPa of H_2 in 5 h [14], satisfying the requirement for the use of H_2 in PEFC.

The fresh Cu-spheroidal ZnO photocatalysts were investigated by Cu K-edge X-ray absorption near-edge structure (XANES) spectroscopy (Fig. 4A-a). The Cu valence state was II in fresh Cu-spheroidal ZnO [14, 28, 35–39]. After illumination for 1 min under UV–visible light, a weak shoulder peak appeared at 8983.1 eV (Fig. 4A-b); the intensity of this peak gradually increased to 0.072 7 compared to normalized Cu K absorption edge under UV–visible illumination for 3 h (Fig. 4A-d). One minute after the UV–visible light was removed, the peak intensity decreased by 0.003 5 (Fig. 4A-e).

The background and peak intensities at 8983.1 eV for Cu^{II} sites (100 %) and Cu^{I} sites (100 %) are indicated by dotted lines in Fig. 4B. The shoulder peak at 8983.1 eV originates from Cu^{I} sites [36–40]. Therefore, the Cu^{I}-site ratio in the sample was evaluated using the following equation:

$$\text{Cu}^{\text{I}}\,\text{site ratio} \sim \frac{\text{Peak intensity@8983.1 eV} - 0.048(\text{for Cu}^{\text{II}}\ 100\,\%)}{0.21(\text{for Cu}^{\text{I}}\ 100\,\%) - 0.048(\text{for Cu}^{\text{II}}\ 100\,\%)}. \tag{16}$$

Based on Eq. 16, the population of Cu^{I} sites gradually increased to 15.6 % after 3 h of UV–visible illumination (Fig. 4B). The growth rate of Cu^{I} sites under UV–visible illumination was 4.1 μmol-Cu h^{-1} g_{cat}^{-1}, which is significantly lower than the photo-PROX rate of CO under similar reaction conditions (84 μmol-CO h^{-1} g_{cat}^{-1}, Table 1h). Thus, the accumulated electrons originally generated in the photocatalyst by light and diffused to Cu^{II} sites should be

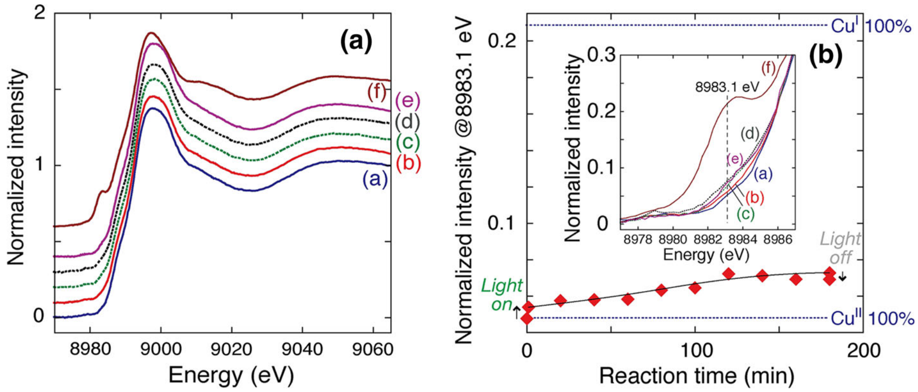

Fig. 4 **A** Normalized Cu K-edge XANES spectra for Cu-spheroidal ZnO *a* before illumination and at *b* 1 min, *c* 80 min, and *d* 180 min from beginning of illumination by UV–visible light with initial pressures of CO (135 Pa), O_2 (270 Pa), and H_2 (13.1 kPa), and *e* at 1 min after the illumination and for *f* Cu-spheroidal ZnO-reduced. **B** Intensity change of shoulder peak at 8983.1 eV during illumination by UV–visible light and intensity for as-prepared Cu-spheroidal ZnO (Cu^{II} 100 %) and Cu-spheroidal ZnO-reduced (Cu^{I} 100 %). *Inset* Enlarged pre-edge region of spectra in panel A [14]. Copyright (2012) Elsevier

detected, whereas the electrons that were transferred from the Cu sites to O_2-derived species for CO PROX reaction should be subtracted [14]. Similarly, the reduction step from Cu^{II} sites to Cu^{I} was also successfully monitored based on the decrease in the peak intensities of the Cu 1s-3d pre-edge peaks for layered double hydroxides during the CO_2 photoreduction steps [41–43].

The anisotropic effects of nano-designed ZnO crystallites on CO PROX activity have also been reported [28]. The CO removal rates and conversions decreased in the following order (Table 1j–m):

$$\begin{aligned}&\mathrm{Cu(0.10\,\%)\text{-}spheroidal\,ZnO} > \mathrm{Cu(0.50\,\%)\text{-}spheroidal}\\&\quad\mathrm{ZnO} > \mathrm{Cu(0.50\,\%)\text{-}disk\text{-}like\,ZnO}\\&\quad\gg \mathrm{Cu(0.32\,\%)\text{-}rod\text{-}like\,ZnO}.\end{aligned} \tag{17}$$

The CO photo-PROX selectivity was higher than 96 % for all the Cu–ZnO photocatalysts. Using XANES, researchers compared the photoreduction rates of Cu sites among Cu-disk-like ZnO, Cu-spheroidal ZnO, and Cu-rod-like ZnO irradiated by UV–visible light. During the irradiation, the intensity of a shoulder peak that occurred at 8983.1 eV in the spectra of all of the Cu-ZnOs gradually increased. The Cu^{I} site ratio was evaluated based on Eq. 16. Assuming first-order reaction kinetics for the reduction

$$[\mathrm{Cu^{II}}] = [\mathrm{Cu^{II}}]_{\mathrm{initial}}e^{-k_{\mathrm{Cu\,reduction}}t}, \tag{18}$$

the rate constant $k_{\mathrm{Cu\ reduction}}$ was determined to be 0.0082, 0.0076, and 0.0032 min^{-1} for Cu-disk-like ZnO, Cu-spheroidal ZnO, and Cu-rod-like ZnO, respectively (Fig. 5) [28]. These values were compared to CO PROX rates of 59, 82, and 16 μmol-CO h^{-1} g_{cat}^{-1} for first-order CO PROX rate constants of 0.017, 0.025, and 0.0021 min^{-1}, respectively. Thus, the $k_{\mathrm{Cu\ reduction}}$ value for the photocatalyst was a general evaluation factor of CO PROX activity.

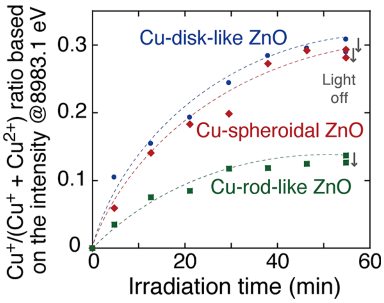

Fig. 5 Intensity change in shoulder peak at 8983.1 eV in normalized Cu K-edge XANES during irradiation by UV–visible light for Cu-disk-like (*filled circle*), Cu-spheroidal (*filled diamond*), and Cu-rod-like ZnOs (*filled square*) [28]. Copyright (2015) American Chemical Society

A photo-PROX reaction begins from a monodentate formate species A [44] (Scheme 2A1 → 2; 4 → 5) that is oxidized by photogenerated holes (Scheme 2A2 → 3; 5 → 6); surface Cu^{2+} sites, which populate preferentially on unsaturated ZnO{1011} faces, are reduced by photogenerated electrons (Scheme 2A2 → 3; 5 → 6) [28]; and O_2 is reduced by electrons via Cu-ion trapping sites coupled with protons of oxidized monodentate formate H^+CO_2 across the crystalline face boundary (Scheme 2A3 → 4 → 5 → 6 → 7) to regenerate two surface hydroxy groups (Scheme 2A7 → 1). In the case of Cu-spheroidal ZnO (see the Graphical abstract), the monodentate formate on the $(000\bar{1})$ face and the Cu sites on the $\{10\bar{1}1\}$ face should be in close proximity, enabling proton transfer (Scheme 2A3, A6) and hydroxy restoration (Scheme 2A7 → 1). The proposed mechanism that includes proton transfer from formate species is closely related to the CO PROX mechanism on a Au/

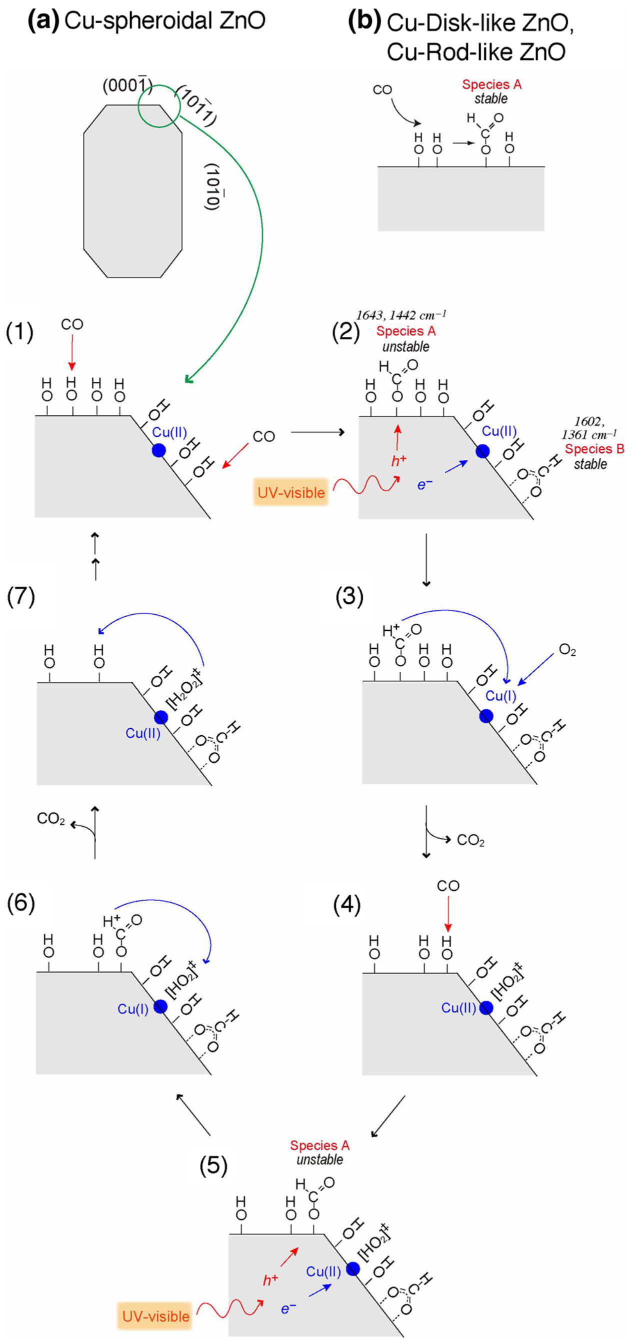

Scheme 2 Proposed surface reaction steps for photo-PROX reaction of CO in H_2 via monodentate formate **A** and route to accumulate inactive bridging formate **B** for Cu–ZnOs [28]. Copyright (2015) American Chemical Society

TiO_2 catalyst, whereas proton transfer from carboxy intermediate on Au is proposed in Sect. 3.1 (see below).

In summary, semiconductor-type photocatalysts based on typical semiconductors such as TiO_2 or ZnO that consist of Ni or Cu ion sites enabled CO photo-PROX reactions at rates of 16–97 µmol h^{-1} g_{cat}^{-1}; these rates are similar to those achieved using molecule-like photocatalysts containing Mo or Cr. Both types of photocatalysts exhibited satisfactorily high CO photo-PROX selectivity of 96–100 %. The participation of hydroxy group was suggested for photocatalytic CO PROX on semiconductor-based catalysts. H_2 is not activated on these photocatalysts and enabled higher CO PROX selectivity in clear contrast to thermal PROX using Au, Co, Cu, or Ni.

3 Thermal PROX Reactions of CO

3.1 Thermal PROX Using Noble Metals

3.1.1 Comparison of Noble Metals

Thermal oxidation of CO has been studied using supported noble metals, e.g., Pt, Pd, Rh, and Au [9]. Pt, Pd, or Rh on Al_2O_3 or Au on Fe oxide [8–11], as well as Ru/TiO_2 (Table 4A, entry d) [45], Ru/Al_2O_3 [46], and Ru/SiO_2 + additives [47, 48], are known to be good catalysts. Comparisons of Pt, Pd, Ru, and Rh supported on either Al_2O_3 or SiO_2 revealed that Ru/Al_2O_3 and Rh/Al_2O_3 exhibited the best performance with respect to CO PROX activity and selectivity [9]. Furthermore, highly-dispersed Au nanoparticles on TiO_2 or on other reducible metal oxides such as Co_3O_4 and CeO_2 (Fig. 6), are highly active toward CO oxidation at temperatures lower than those required for Pt catalysts [9, 49]. Reducible metal oxides have been proposed to transfer electrons to Au nanoparticles leading to the reduction reaction over the surface [50]. The CO oxidation rate in balance N_2 gas (not CO PROX) at a relatively suppressed flow rate of 17 mL min^{-1} in the presence of Au/TiO_2 was sufficiently fast: 72 000 µmol h^{-1} g_{cat}^{-1} (Table 4A, entry k) [51]. The CO PROX performance of Au catalysts on reducible metal oxides, e.g., TiO_2, Fe_2O_3, Co_3O_4, NiO, MnO_2, and CeO_2, has been reviewed elsewhere [9, 10].

The higher reactivity of supported noble metals is great advantage, however, as the nature of supported noble metals, dissociative adsorption of H_2 through free electrons of metals and the following reaction with O_2 are inevitable, especially at increased reaction temperature. The selectivity for CO PROX compared to H_2 oxidation decreased rapidly with increasing flow rates of the reactants and with increasing reaction temperature [8–10]. At higher temperatures, weaker CO adsorption and/or a competing H_2 oxidation reaction was suggested to cause the decrease in PROX selectivity on Au catalysts. To clarify the dependence of CO PROX on the flow rates of the reactants and on the reaction temperature, we focus on the PROX mechanism of CO on Au catalysts in the next section.

In summary, supported Ru, Rh, Pt, and Au catalysts, especially those supported on reducible metal oxides, exhibit excellent CO PROX rates of 1000–4900 µmol h^{-1} g_{cat}^{-1}. The

Table 4 Comparison of rates of thermal-PROX or oxidation reactions of CO reported in literature

Entry	Catalyst		T (K)	Light	System	Reactants P	$R_{CO \to CO2}$ (μmol h^{-1} g_{cat}^{-1})[1]	$T_{50\%}$ (K)[2]	CO Conv. (%)[3]	CO_2 Selec. (%)[4]	Ref.
	Type	W (mg)									
(A) Comparison using noble metals versus inexpensive metals											
a	Mn(5 %)/TiO_2	200	353	No	Flow (75 mL min^{-1})	CO 1.0 kPa, O_2 1.0 kPa, H_2 61 kPa	200	>453 K	2.1	81	[45]
b	Co(5 %)/TiO_2						320	405	3.4	90	
c	Cu(5 %)/TiO_2						620	399	6.6	~100	
d	Ru(1 %)/TiO_2						4700	353	50	37	
e	Pd(1 %)/TiO_2						~0	>453 K	~0	~0	
f	Ag(1 %)/TiO_2						220	>453 K	2.3	63	
g	Ir(1 %)/TiO_2						630	>453 K	6.7	92	
h	Pt(1 %)/TiO_2						1000	>453 K	11	36	
i	Au(1 %)/TiO_2						~0	>453 K	~0	78	
j[5]	Pt(1.0 %)/TiO_2	50	300		Flow (17 mL min^{-1})	CO 1.0 kPa, O_2 21 kPa, N_2 78 kPa	680	339		–	[51]
k[5]	Au(3.1 %)/TiO_2						72,000	235			
l	Pt/γ-Al_2O_3	50	373		Flow (100 mL min^{-1})	CO 1.0 kPa, O_2 1.3 kPa, H_2 51 kPa	2500	434	5.0	49	[60]
m	Au/α-Fe_2O_3						49,000	310	97	48	
n	CuO–CeO_2						32,000	367	63	~100	
o	Pt/γ-Al_2O_3				Flow (21 mL min^{-1})		2100	444	20	44	
p	Au/α-Fe_2O_3						10,000	<303	95 @353 K	39 @353 K	
q	CuO–CeO_2						10,000	345	96	~100	
r	Au(2.0 %)/TiO_2	200	323		Flow (100 mL min^{-1})	CO 0.5 kPa, O_2 0.5 kPa, H_2 86 kPa	4800			36	[63]
s				4 W UV lamp × 4			5000			38	

Table 4 continued

Entry	Catalyst		T (K)	Light	System	Reactants P	$R_{CO\rightarrow CO2}$ (μmol h^{-1} g_{cat}^{-1})[1]	$T_{50\%}$ (K)[2]	CO Conv. (%)[3]	CO_2 Selec. (%)[4]	Ref.
	Type	W (mg)									
t	Au(1.0 %)/TiO_2	500	298	No	Flow (100 mL min^{-1})	CO 0.3 kPa, O_2 0.3 kPa, H_2 81 kPa	260		18	66	[65]
u				300 W Xe (490 < λ<760 nm)			360		24	68	
v	Au(1.0 %)-polyaniline(4.7 %)/ TiO_2			No			690		47	75	
w				300 W Xe (490 < λ<760 nm)			770		52	81	
x	Au(1.0 %)–CuO(10 %)/TiO_2			No			820		55	76	[66]
y				300 W Xe (490 < λ<760 nm)			1000		70	85	
z	Au(0.5 %)/TiO_2	700	293	No	Flow (100 mL min^{-1})	CO 0.3 kPa, O_2 0.3 kPa, H_2 86 kPa	320		30	67	[67]
α				300 W Xe (490 < λ<760 nm)			400		37	68	
β	Au(0.5 %)/Al_2O_3			No			250		24	93	
γ				300 W Xe (490 < λ<760 nm)			270		25	89	

Entry	Catalyst		T (K)	System	Reactants P	$R_{CO\rightarrow CO2}$ (μmol h^{-1} g_{cat}^{-1})[1]	$T_{50\%}$ (K)[2]	CO Conv. (%)[3]	CO_2 Selec. (%)[4]	Ref.
	Type	W (mg)								
(B) *Comparison using inexpensive transition metals*										
a	CuO(5 %)–SiO_2	250	513	Flow (40 mL min^{-1})	CO 1.0 kPa	2200		6.7	–	[69]
b	CuO(5 %)–TiO_2		363		O_2 1.0 kPa	2300		7.0		
c	CuO(5 %)–CeO_2		343		N_2 98 kPa	1700		5.4		
d	CuO–CeO_2	100	373	Flow (100 mL min^{-1})	CO 1.0 kPa, O_2 0.51 kPa, H_2 51 kPa	19,000	360	75	99	[70]
e	CnO–CeO_2 (Cu/Ce = 1/1.7)	200	333	Flow (30 mL min^{-1})	CO 4.0 kPa O_2 10 kPa N_2 86 kPa	1500		9.5	–	[72]

Table 4 continued

Entry	Catalyst		T (K)	System	Reactants P	$R_{CO\rightarrow CO2}$ (μmol h^{-1} g_{cat}^{-1})[1]	$T_{50\%}$ (K)[2]	CO Conv. (%)[3]	CO_2 Selec. (%)[4]	Ref.
	Type	W (mg)								
f	$CuO–CeO_2$ (Cu/Ce = 1/4)		323	Flow (1000 mL min^{-1} g_{cat}^{-1})	CO 1.0 kPa,	4400	330	17	48	[73]
					O_2 1.25 kPa,					
					H_2 50 kPa					
g	$CuO–CeO_2$–NR	400	343	Flow (2000 min^{-1})	CO 1.0 kPa		360	11	–	[78]
h	$CuO–CeO_2$–NS				O_2 2.0 kPa		400	1.5		
					N_2 97 kPa					
i	$CuO–CeO_2$–NS		343	Flow (500 mL min^{-1} g_{cat}^{-1})	CO 1.0 kPa,	2700	359	20	100	[79]
j	$CuO–CeO_2$–NR				O_2 1.25 kPa,	5400	353	40	80	
k	$CuO–CeO_2$–NC				H_2 50 kPa	1300	373	10	83	
l	CuO(4 %)–CeO_2	300	373	Flow (600 mL min^{-1})	CO 0.50 kPa,	9000	347	33.5	100	[74]
					O_2 0.50 kPa,					
					H_2 50 kPa					
m	$CuMn_2O_4$	15–30	423	Flow (200 mL min^{-1})	CO 0.51 kPa,		427	42	84	[81]
n	$CuO–CeO_2$				O_2 0.51 kPa,		454	18	91	
					H_2 25 kPa					
o	Cu–Mn (1:2) oxide	50	373	Flow (50 mL min^{-1})	CO 1.0 kPa,	19,000	351	74		[82]
p			333		O_2 1.0 kPa,	7100		28		
q[6]	Hopcalite 8-14#		373		H_2 61 kPa	16,000	366	63		
r[6]			333			5100		20		
s	Cu-Fe-$K_{2x+y}Mn^{II}_{x}Mn^{III}_{y}Mn^{IV}_{8-x-y}O_{16}$	100	373	Flow (100 mL min^{-1})	CO 2.0 kPa,	14,000	391	27	91	[83]
					O_2 1.0 kPa,					
					H_2 51 kPa					
t	CuO(17 %)–ZnO(46 %)–TiO_2(37 %)		363	Flow (18,000 h^{-1})	CO 1.2 kPa,		381	32	~100	[84]
					O_2 1.2 kPa,					
					H_2 51 kPa					
u	Co–Mn (8:1) oxide nanosheet	100	333	Flow (25 mL min^{-1})	CO 1.0 kPa,	6300	<303	98	90	[87]
v	Co–Mn (8:1) oxide/FeO_x	200	348	Flow (50 mL min^{-1})	O_2 1.0 kPa,	6300	<303	~100		[88]
					H_2 51 kPa					
w	Co_3O_4(20 %)–$Ce_{0.85}Zr_{0.15}O_2$	100–200	373	Flow (250 mL min^{-1} g^{-1})	CO 1.0 kPa,		383	36	~100	[89]
					O_2 1.0 kPa,					
					H_2 51 kPa					
x	Co(8.4 %)–CeO_2		373	Flow (2.1 mg mL^{-1} min)	CO 1.0 kPa,		392	22	~100	[90]
y	Mn(9.9 %)–Co(10 %)–CeO_2				O_2 1.0 kPa,		377	41	~100	
z	Mn(0.94 %)/CeO_2				H_2 41 kPa		451	2	~100	

Table 4 continued

Entry	Catalyst		T (K)	System	Reactants P	$R_{CO \to CO2}$ (μmol h^{-1} g$_{cat}^{-1}$)[1]	$T_{50\%}$ (K)[2]	CO Conv. (%)[3]	CO_2 Selec. (%)[4]	Ref.
	Type	W (mg)								
α[7]	Co–OMS(Mn)	40	373	4.3 mL min^{-1}	CO 1.0 kPa,	11,000		91.1	~100	[91]
β[7]	Cu–OMS(Mn)				O_2 0.51 kPa,	6700		76.4	~100	
					H_2 30 kPa					
γ	Co_3O_4	30	373	Flow (200 mL min^{-1})	CO 0.51 kPa,	15,000	398	17	81	[86]
					O_2 0.51 kPa,					
					H_2 25 kPa					
δ	Co(10 %)–ZrO_2	200	373	Flow (25 mL min^{-1})	CO 0.51 kPa,	1300	356	81	91	[92]
ε				Flow (50 mL min^{-1})	O_2 0.51 kPa,	1700	368	53	87	
					H_2 5.1 kPa					
ζ	Co(3.2 %)–$SrCO_3$	120	513	Flow (32 mL min^{-1})	CO 1.0 kPa,			96	68	[93]
					O_2 0.51 kPa,					
					H_2 95 kPa					
η	$NiFe_2O_4$	100	473	Flow	CO 1.0 kPa,			9.1	68	[94]
					O_2 1.0 kPa,					
					H_2 71 kPa					
θ	CuO–CeO_2 (Cu:Ce = 1:5)	100	323	Flow (20 mL min^{-1})	CO 0.5 kPa,	710		28	96	[102]
ι	Cu–MIL125 (Cu:Ti = 1:2)				O_2 0.5 kPa,	1900		76	99	
					H_2 50 kPa					
κ	Au(5.0 %)/TiO_2	10	293	Closed circulation	CO 63 Pa,	1200		100 @1 h	93	[14]
					O_2 150 Pa,					
					H_2 6.3 kPa					
λ	CuO–CeO_2 (Cu:Ce = 1:5)	50	323	Closed circulation	CO 63 Pa,	140		98 @1 h	90	[102]
μ	Cu–MIL125 (Cu:Ti = 1:2)				O_2 150 Pa,	140		97 @1 h	98	
					H_2 6.3 kPa					

W sample weight charged, T reaction temperature, P pressure

[1] $R_{CO \to CO_2}$: CO removal rate

[2] $T_{50\%}$: Temperature at which the CO conversion reaches 50 %

[3] CO Conv.: CO conversion (%) = 100 × $(n_{CO,Start} - n_{CO,End})/n_{CO,Start}$

[4] CO_2 Selec.: CO_2selectivity(%) = $100 \times n_{CO_2}/(n_{CO_2} + n_{H_2O})$

[5] Not PROX but simple oxidation

[6] Hopcalite 8-14# was from GL Sciences Inc., Japan

[7] OMS(Mn): Octahedral molecular sieve comprising Mn

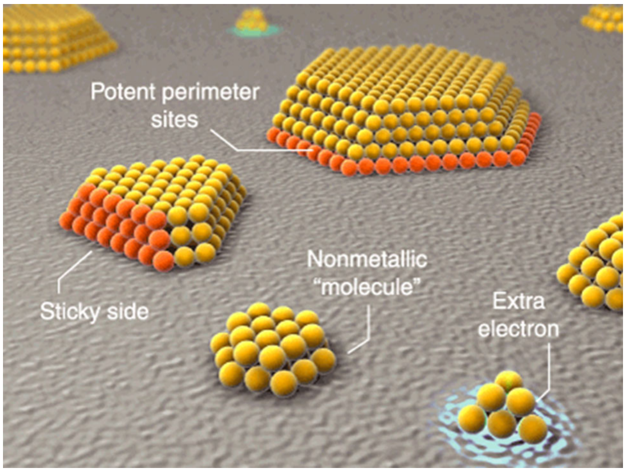

Fig. 6 Plausible models of supported Au nanoparticles designed to explain why ordinarily inert Au turns into powerful catalysts when shrunk to nanoparticle dimensions [7]. Copyright (2003) American Association for the Advancement of Science

drawback of these catalysts is that the CO PROX selectivity dramatically decreases with increasing flow rates of the reactants and increasing reaction temperature: 36–48 % at flow rates of 75–100 mL min^{-1} and at 353–373 K due to effective activation of H_2 on noble metal surfaces leading to by-reaction of water formation.

3.1.2 CO PROX (or Oxidation) Mechanisms Using Au Supported on Reducible Oxides

The reason that highly dispersed Au nanoparticles are good catalysts for the CO PROX reaction has been studied by many researchers [7] by designing controlled Au nanoparticles through atom-by-atom architecture of the underlying metal oxide surfaces, e.g., single-crystalline surfaces. These previous studies have typically involved mapping such controlled surfaces using scanning tunneling microscopy and using density functional theory (DFT) to model how atoms and molecules react with Au nanoparticle surfaces and/or the underlying metal oxide surface via a reaction route that minimizes the energy (Fig. 6).

A PROX mechanism was proposed in which CO adsorbs onto metal nanoparticles (e.g., Au on TiO_2) and reacts with O_2 at the boundary between the metal nanoparticles and the support [52–56]. Lower temperature needs to be chosen to avoid H_2 dissociation on Au metal surface instead of CO to guarantee higher selectivity for CO PROX. In particular, Au nanoparticles 2–8 nm in diameter, and most likely 3 nm in diameter, on TiO_2 powder were carefully studied in detail at 110–130 K using IR spectroscopy [52]. In the case of TiO_2 powder under 8.0 Pa of CO at 120 K, the resulting IR spectrum showed an intense, broad peak at 2102 cm^{-1} (chemisorbed CO on metallic Au^0), an intense, sharp peak at 2179 cm^{-1} (adsorbed CO on TiO_2), and a small peak at 2341 cm^{-1} (chemisorbed CO_2 on TiO_2). The CO_2 was formed from CO by reaction with a trace amount of O_2 that remained in the IR cell.

When 130 Pa of O_2 was introduced at 120 K, the amount of CO on TiO_2 gradually decreased, whereas the amount of CO_2 on TiO_2 increased over a period of 20 min (Scheme 3). In clear contrast, the amount of CO on Au^0 decreased very slowly: only 12 % conversion in 120 min. CO oxidation negligibly proceeded on TiO_2 free from Au, indicating the critical role of Au sites. The reaction was first-order, and the apparent activation energy was evaluated to be 15 kJ mol^{-1} ± 1 kJ mol^{-1} at 110–130 K. The rate dependence on O_2 pressure was 0.5th order at 120 K and suggested that the Au/TiO_2 surface was saturated at an O_2 pressure of 330 Pa.

When the CO-adsorbed Au/TiO_2 was heated to 215 K, CO on TiO_2 totally desorbed, whereas half of the CO on Au^0 remained. The sample was again cooled to 120 K and interacted with 130 Pa of O_2, but was inactive toward CO oxidation. Although the reason for the increase in intensity of the weak, broad peak at 2353 cm^{-1} was not mentioned [52], CO on Au should migrate to TiO_2 and be oxidized to CO_2. In any event, it was observed that CO on TiO_2 was likely more reactive with O_2 compared to that on Au^0; however, the oxidation required the participation of Au.

In this context, gradient-corrected DFT calculations were performed for three layers of Au nanorods over a rutile-type $TiO_2(110)$ surface, and the plausible reaction at the interface was closely evaluated. CO adsorbed onto TiO_2, and O_2 was stable in a di-σ configuration with bonds

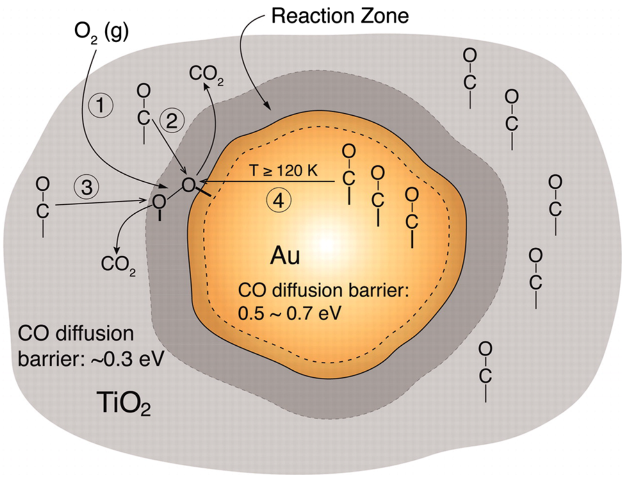

Scheme 3 Proposed mechanism of low-temperature CO oxidation over Au/TiO_2 catalyst at boundary zone between Au nanoparticle and TiO_2. Experiments directly observing CO/TiO_2 and CO/Au surface species showed that processes 2 and 3 were fast compared to process 4 [52]. Copyright (2011) American Association for the Advancement of Science

to both Ti_{5c} (five-coordination to O atoms) sites and with Au atoms at the interface (Scheme 3①). The activation barrier for diffusion of CO to the Ti_{5c} site in proximity to Au (Scheme 3②) was 25 kJ mol^{-1} and may be rate-determining as compared to the experimental apparent activation energy of 15 kJ mol^{-1}. At temperatures greater than 110–130 K, CO diffusion from Au to the interface with TiO_2, for which the activation barrier is 48 kJ mol^{-1} (Scheme 3④), is also plausible.

This study enabled the adsorption and diffusion of CO on TiO_2 surface at low temperature (120 K) and the reaction with O_2 at the interface sites with Au nanoparticle. The proposed mechanism in most studies was confirmed at higher than 120 K.

The O_2 activation site at the interface between Au and its metal oxide support was further investigated based on kinetic measurements utilizing isotope effects and DFT calculations [53]. In cases in which the support material lacked surface hydroxy groups, e.g., C and g-C_3N_4, the composites with Au were inactive [56, 57]. Furthermore, in contrast to the site-blocking effect of water on CO photooxidation catalysts (see the Sect. 2.2.2) [17] and Cu or Co catalysts supported on reducible metal oxides (see the Sects. 3.2.2, 3.2.3, 3.2.4 and Table 3), the presence of water enhanced the CO photooxidation rates by a factor of 6.8 [53] or 32 [58]. When the surface hydroxy group of the Au/TiO_2 catalyst was deuterated (surface O^2H groups), the CO oxidation rate decreased by a factor of 0.56 compared to that achieved using a non-deuterated Au/TiO_2 catalyst with surface O^1H groups, suggesting a primary isotope effect in which the O–^{1}H (^{2}H) bond cleavage was rate-determining and the initial state zero-point energy affected the activation efficiency.

When the Au/TiO_2 catalyst was dried at 343 K for 16 h, 97 % of the area of the non-H-bonded hydroxy peak at 3741–3645 cm^{-1} remained, whereas the area of the water peak in the IR spectrum substantially decreased. The CO oxidation rates decreased by a factor of 0.094 as a consequence of the drying. Furthermore, the reaction order for the moisture pressure was 0.32, which was substantially greater than that for CO (0.01) or O_2 (0.1). The dependence of the reaction rates on the partial pressures of O_2 and moisture was compared to the Michaelis–Menten kinetics model [59]:

$$\upsilon^{-1} = \frac{K_m}{\upsilon_{\max}} P_{O_2} + \upsilon_{\max}^{-1} \tag{19}$$

As P_{H_2O} was increased from 1 Pa to 125 Pa, the variation of the value of K_m/v_{max} was small whereas v_{max}^{-1} substantially decreased (i.e., the reaction rate increased). Thus, weakly-adsorbed water increased the effective number of active sites instead of modifying their inherent activity. Rather than direct participation of hydroxy groups in the reaction mechanism, hydroxy groups were hypothesized to anchor water molecules near the Au nanoparticle and facilitate the activation of water through H bonding. Furthermore, the reaction between O_2 was stabilized by proton transfer (Au–OOH) from Au–CO to Au–O and Au–CO_2H through a low activation barrier (9.6 kJ mol^{-1}; Fig. 7A②).

In summary, this paper successfully explained the plausible intermediates of promoted CO oxidation in the presence of moisture. O–O bond scission was suggested by the formation a CO–O_2 complex at the interface between Au nanoparticles and TiO_2 according to the results of IR and DFT studies. Furthermore, an H/D (^{2}H) kinetic isotope effect of nearly 2 suggested that the O–H(D) bond scission step was rate-determining. The v_{max} value increased linearly with the amount of adsorbed water by changing the number of active sites and adsorbed water also stabilized the intermediate species (Au–OOH, Au–COOH) to form CO_2.

3.1.3 *Comparisons of Effects of CO_2 and/or Moisture in Reactant Gas*

The $T_{50\%}$ value is the temperature at which the CO conversion reaches 50 % and the criteria of higher CO PROX activity as the value decreases. For practical applications, the effects of CO_2 and moisture contained in real reactant gas for CO PROX reactions are critical. The $T_{50\%}$ values for Au/α-Fe_2O_3 (310 K), CuO–CeO_2 (367 K), and Pt/γ-Al_2O_3 (434 K) (Table 4A, entries l–n and Fig. 8) increased to 350 K, 389 K, and 440 K, respectively, after the addition of 10 % of CO_2 into the feed gas at a reactant flow rate of 100 mL min^{-1} (Table 2d–f; Fig. 8) [60]. More active Au/α-Fe_2O_3 and CuO–CeO_2 were dramatically affected by the added CO_2, whereas the effect of CO_2 on relatively inactive Pt/γ-Al_2O_3 was marginal. The CO_2 selectivity was not substantially affected by the presence of CO_2 (Tables 2d–f, 4A-l–n) demonstrating that the mechanism was not altered by CO_2 but the frequency factor of reaction was suppressed by CO_2. At 373 K, Au/α-Fe_2O_3 was the most active, whereas CuO–CeO_2 was the most selective to CO_2.

The $T_{50\%}$ values for Au/α-Fe_2O_3 (301 K), CuO–CeO_2 (368 K), and Pt/γ-Al_2O_3 (398 K) by the addition of 10 % of CO_2 in the feed gas changed to 341 K, 414 K, and 377 K, respectively, by the addition of both 10 % of CO_2 and 15 % of moisture in the feed gas at a flow rate of 21 mL min^{-1} (Tables 2g–i, 4A-o–q) [60]. A negative effect of moisture was apparent for more active Au/α-Fe_2O_3 and CuO–CeO_2, whereas promotion was observed for Pt/γ-Al_2O_3. Promoting effect of weakly adsorbed water to stabilize Au–OOH and/or Au–COOH intermediate and enhance the frequency of simple CO oxidation in previous section, but the promoting effect of moisture at much lower partial pressure of 1–700 Pa was observed for Au/TiO_2 in reference 53 versus negative effect by the addition of much higher 10 kPa of moisture was confirmed for Au/α-Fe_2O_3 in reference 60. As the comparisons in reference 60 were made below the onset temperature of the WGSR (418 K), the promotion effect of CO oxidation by water using Pt/γ-Al_2O_3 was net and not due to the balance for rates of by-reaction(s).

In summary, at practical temperature range for CO PROX reactions (353–473 K), the addition of CO_2 and/or moisture in PROX gas of CO deactivated for both supported noble metals (Au, Pt) and CuO–CeO_2 catalysts by 6–46 K of $T_{50\%}$ except for the promotion of Pt/γ-Al_2O_3 by moisture (−21 K of $T_{50\%}$). The Pt catalyst was quite inactive compared to the other two catalysts, marginal step at very low temperature for Pt was improved and the mechanism would be unimportant for highly active catalysts.

3.1.4 *Photoassisted PROX Using Au Catalysts*

Photocatalysis involving CO as product using noble metals supported on TiO_2 and other metal oxides is widely used for, e.g., the photoconversion of CO_2 into fuels [3, 13, 61]. The conversion of CO_2 is endothermic [62], and one plausible CO_2 photoconversion reaction is the reverse WGSR (reverse reaction of Eq. 1):

$$H_2 + CO_2 \rightleftarrows H_2O + CO. \tag{1'}$$

By contrast, CO PROX reactions are exothermic and often proceed at 293–323 K in the presence of noble metals, even without irradiation by light; indeed, the contribution of light energy for these noble metal catalysts is not always clearly discussed in literature. Such cases are referred to as "photoassisted PROX" and we try to separate the contributions of thermal and photocatalysis in this section.

Photoassisted PROX using Au/TiO_2 and promoted by irradiation has been reported. Under a flow of 0.5 % of CO + 0.5 % of O_2 + 85 % of H_2 + balance gas and in the absence of light, the CO PROX rate was quite high (4800 μmol h^{-1} g_{cat}^{-1}; Table 4A, entry r) using Au/TiO_2 catalyst. Under irradiation by UV light at 323 K, the rate increased by a factor of 1.04, although the PROX selectivity was low (36–38 %) at a reactant flow rate of 100 mL min^{-1} in both the presence and absence of light (Table 4A, entries r and s) [63]. Based on CO PROX reaction mechanism proposed in Sect. 3.1.2 [52, 53], the electrons separated from holes in TiO_2 irradiated by UV light would diffuse to Au and then to O_2 adsorbed at the interface between Au and TiO_2 [41, 43]. Hot electrons induced by surface plasmon resonance (SPR) [64] on Au nanoparticles irradiated by visible light would also diffuse to the O_2 [41, 43]. However, the promotion of electron injection into Au then to O_2 by the effect of light was marginal (4 %) in the case of Au/TiO_2 catalyst because the free electrons of Au would be sufficient at the interface between Au nanoparticles and TiO_2. A lower reaction temperature and/or lower flow rate was necessary to achieve better PROX selectivity.

In the case of an Au/TiO_2 catalyst assembled with polyaniline with the aim to respond to visible light, the CO PROX rate increased by a factor of 2.1 (770 μmol h^{-1} g_{cat}^{-1}) under visible-light irradiation compared to that without polyaniline (Table 4A, entries u and w) [65]. The electron transfer initially excited in polyaniline by visible light toward TiO_2 should be the reason for the observed increase. The superior performance of polyaniline-assembled Au/TiO_2 catalyst (690 μmol h^{-1} g_{cat}^{-1}) to Au/TiO_2 under dark conditions (260 μmol h^{-1} g_{cat}^{-1}; Table 4A, entries t and v) is attributable to charge transfer from the polyaniline to the TiO_2 rather than to charge separation by light.

The PROX activity of Au/TiO_2 modified with CuO was also tested in the presence/absence of visible light [66]. Because of the effects of CuO, which are likely electronic effects, the rate achieved using Au-CuO/TiO_2 (820 μmol h^{-1} g_{cat}^{-1}) under dark conditions increased by a factor of 3.2 compared to that observed using Au/TiO_2 (260 μmol h^{-1} g_{cat}^{-1}) under the same conditions (Table 4A, entries t and x). Both catalytic reactions were promoted to a similar extent by irradiation with visible light: the rate in the case of Au–CuO/TiO_2 increased by a factor of 1.22 times (1000 μmol h^{-1} g_{cat}^{-1}), whereas that in the case of Au/TiO_2 increased by a factor of 1.38 (360 μmol h^{-1} g_{cat}^{-1}; Table 4A, entries t, u, x, and y). The photoassist mechanism is essentially the same as that for reference 63. Separated electrons in TiO_2 by UV light and hot electrons by SPR at Au and/or CuO by visible light would transfer to O_2 adsorbed at the interface between TiO_2 and Au/CuO [41, 43] and accounted for 22–38 % increase of the CO PROX rate.

The CO PROX performance in the case of Au/TiO_2 was compared to that using Au/Al_2O_3 under visible-light irradiation and otherwise similar reaction conditions [67]. The CO conversion using Au/TiO_2 increased from 30 % in the dark to 37 % under irradiation (Table 4A, entries z and α) similar to the mechanism for references 63 and 66. In contrast, the CO conversion using Au/Al_2O_3 was substantially lower (24–25 %), and the effects of visible-light irradiation were not observed because Al_2O_3 is an insulator and cannot induce charge separation (Table 4A, entries β and γ). For both catalysts, the CO PROX selectivity negligibly changed under visible-light irradiation (from 67 to 68 % and from 89 to 93 %, respectively) suggesting electron transfers to adsorbed O_2 both thermal and photocatalytic mechanism led to common reaction paths.

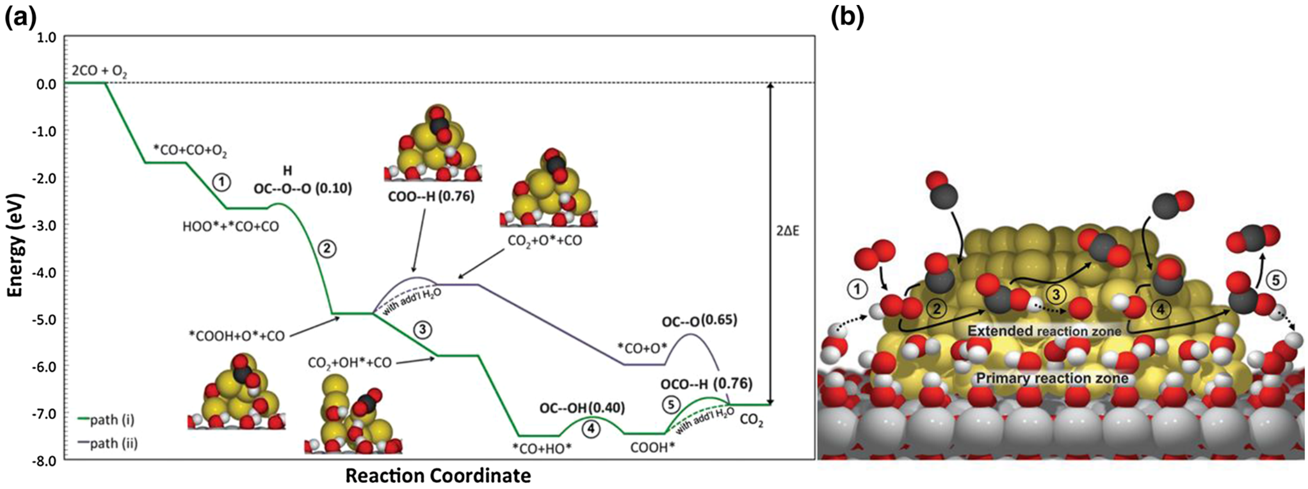

Fig. 7 Proposed reaction mechanism of CO oxidation. Larger *white ball* Ti atom, *red/darker ball* O atom, *gray/darkest ball* C atom, and *smaller white ball* H atom. **a** Potential energy diagram. Both pathways *i*, *ii* proceed through decomposition of COOH intermediate and reaction between CO and OH (or O) intermediates. **b** Schematic of lower pathway *i* (*green/thinner line*) in **a** [53]. Copyright (2014) American Association for the Advancement of Science (Color figure online)

In summary, Au-supported photocatalysts exhibited CO PROX at rates of 270–5000 μmol h^{-1} g_{cat}^{-1}, and comparable rates of 260–4800 μmol h^{-1} g_{cat}^{-1} were achieved even in the absence of light. Electron transfer via thermal process to O_2 at the interface between Au and TiO_2 was dominant and the photoassist via the transfer of photodissociated electrons in TiO_2 to Au then to O_2 at interface was marginal. The CO_2 selectivity was generally low but ranged from 36 to 93 %.

3.2 Thermal PROX Using Inexpensive Elements

3.2.1 Ce-Based Catalysts

CeO_2-based PROX catalysts of CO are known as some of the best-performing PROX catalysts composed without noble metal although Ce is a rare earth metal and not inexpensive; they have been briefly reviewed and CuO–CeO_2 is one of the most studied catalyst [8, 9, 11]. Furthermore, when incorporated as dopants, Fe, Ni, and Sn acted as promoters, increasing the activity and selectivity of CuO–CeO_2 catalysts. Pt increased the activity, but not the selectivity of CuO–CeO_2 catalysts. The incorporation of 10 mol % of ZrO_2 also increased the activity of CuO–CeO_2 catalysts [11]. Efficient mixing of Cu^{2+} and Ce^{4+} sites, which enabled effective utilization of the redox cycle, was established as the origin of the high PROX activity toward CO.

$$CO + Cu^{2+}{-}O{-}Ce^{4+} \rightarrow CO_2 + Cu^{+}{-}[O\,\text{vacancy}]{-}Ce^{3+} \tag{20}$$

As described above for the PROX selectivity, metal oxides, e.g., CuO and CeO_2, are superior to noble metals not to activate H_2 in CO PROX reaction tests. The presence of water and CO_2 in the feed gas retarded the PROX reaction substantially [8].

Optimization of the performance of Ce-based catalysts was already reported to explain why CuO–CeO_2 catalysts have been most intensively studied. The catalytic performance for CO PROX conversion and selectivity using inexpensive transition metals—Cr, Co, Ni, Cu, or Zn—on $Ce_{0.63}Zr_{0.37}O_2$ decreased in the order [9, 68]

$$Cu > Ni > Co > Zn > Cr. \tag{21}$$

In the case of Cu, the performance depending on support material decreased in the order [9, 68]

$$CeO_2 > La_2O_3 > MgO > SiO_2{-}Al_2O_3. \tag{22}$$

The active sites of CuO–CeO_2 catalysts were the well-mixed Cu and Ce oxides, ideally mixed on the atomic level to enable Eq. 20, and excessive Cu in the form of segregated CuO species led to the inactivation [9].

In summary, CuO–CeO_2 is systematically the best catalyst for CO PROX reactions owing to the redox of Eq. 20 and polar nature of metal oxide surface to activate CO and O_2 rather than H_2, free from expensive elements such as Ru, Rh, Pt, and Au that would activate H_2 above moderate reaction temperature (~350 K).

3.2.2 Reaction Mechanism over CuO–CeO_2

Kinetics studies have revealed that CO oxidation proceeds on CuO–CeO_2 via the Mars van Krevelen mechanism (see the Graphical abstract). It is specific mechanism to utilize vacancy sites and worthy to be reviewed in relation to CO PROX activity and selectivity. This mechanism includes a

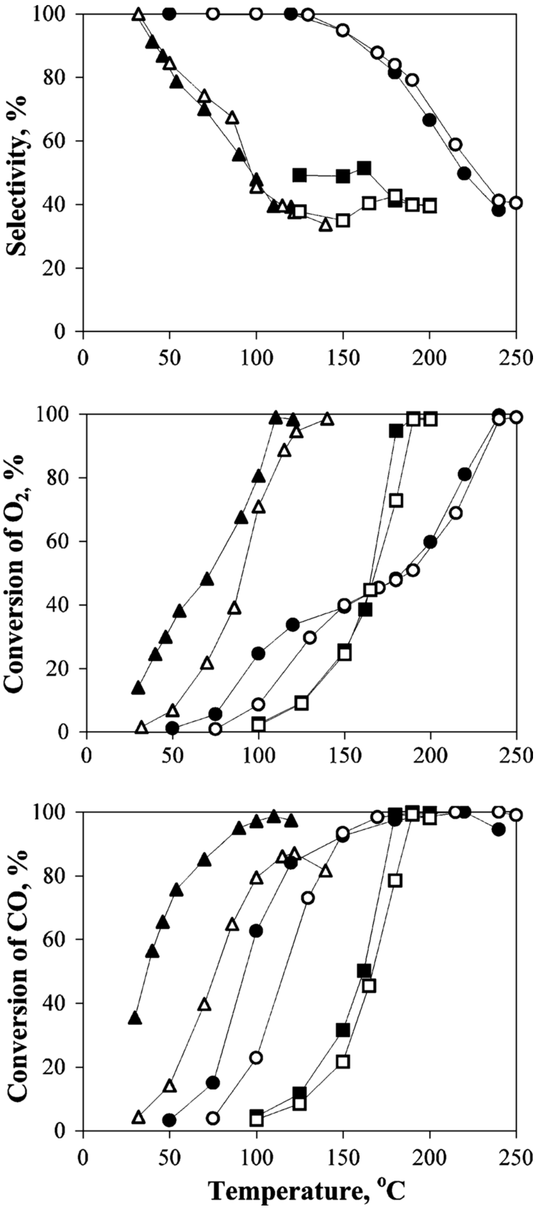

Fig. 8 Changes in CO and O_2 conversion and in CO PROX selectivity versus temperature at (catalyst weight)/(flow rate) = 0.030 g s mL^{-1} over Au/α-Fe_2O_3 (*triangle*), CuO–CeO_2 (*circle*), and Pt/γ-Al_2O_3 (*square*) catalysts in absence of CO_2 (*filled symbols*) and in presence of 15 % CO_2 in reactant feed (*open symbols*) [60]. Copyright (2002) Elsevier

reaction step in which an adsorbed species reacts with lattice O (Scheme 4) [69–71]: a CO molecule adsorbs onto CuO (Eq. 23) and reacts with a lattice O atom at the boundary between CuO and CeO_2 (Eq. 24), resulting in CO_2 formation and leaving an O vacancy site on the CeO_2 surface (Eq. 24). An O_2 molecule then fills the O vacancy (Eq. 25):

$$CO + Cu \rightleftarrows Cu{-}CO, \tag{23}$$

$$Cu{-}CO + (\text{lattice O}) \rightleftarrows Cu + CO_2 + (\text{vacant lattice}), \tag{24}$$

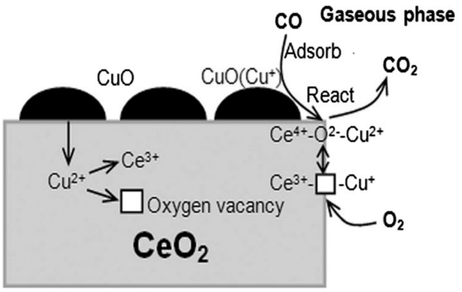

Scheme 4 Proposed reaction mechanism of CO oxidation over CuO–CeO_2 catalyst [72]. Copyright (2015) The Royal Society of Chemistry

and

$$O_2 + 2(\text{vacant lattice}) \rightleftarrows 2(\text{lattice O}). \tag{25}$$

The formation of O vacancies involves the reductions of Ce^{IV} to Ce^{III} and of Cu^{II} to Cu^{I} (Eq. 20 and Scheme 4), as confirmed by X-ray photoelectron spectroscopy (XPS) [70, 72]. With respect to the reduction, the correlation between the peak intensity of Cu^{I}–CO in diffuse-reflectance infrared Fourier transform (DRIFT) spectra and CO PROX activity was confirmed. CO adsorbed onto Cu^{I} sites, whereas H_2 preferably adsorbed onto metallic Cu sites. Therefore, the oxidation sites for H_2 and CO were independent and enabled high CO PROX selectivity if the Cu sites were kept as oxidized [71].

As described in Sect. 3.2.1, the reducibility of Cu^{II} to Cu^{I} and of Ce^{IV} to Ce^{III} was essential for CO PROX using CuO–CeO_2 catalysts [73–76]. The specific interface sites between CuO and CeO_2 were investigated by H_2 temperature-programmed reaction (H_2-TPR), CO-TPR, and temperature-programmed oxidation [74]. Reduction of CuO–CeO_2 by H_2 occurred at 433 K, 380 K lower than the H_2 reduction temperature of CeO_2 (813 K). The CuO sites at the CuO–CeO_2 interface were reduced by CO and reoxidized by O_2 at 290–423 K in consistent with Scheme 4. At temperatures above 423 K, Cu^{II} both at the interface sites and at other sites began to be deeply reduced (namely to Cu^{0}) by H_2. The deeply-reduced Cu sites were reoxidized by O_2; however, the catalysts exhibited only low CO PROX selectivity.

The correlation between Cu valence states and CO PROX performance was investigated using CuO–CeO_2 by in situ XANES [73]. At temperatures below 390 K, the CO oxidation reaction was predominant and the Cu oxidation state was II. In the temperature range from 390 to 470 K, H_2 began to be oxidized, coupled with the partial reduction of Cu^{II} to Cu^{I}. At temperature above 470 K, H_2 oxidation became predominant and inactive Cu_2O and metallic Cu particles accumulated. Thus, redox between Cu^{II} and Cu^{I} was suggested to participate in CO oxidation (Eq. 24) via the Mars van Krevelen mechanism.

The preferable population of Cu^I sites on each crystal face of CeO_2 was investigated by first-principles calculations. The most stable and preferentially exposed crystalline face of CeO_2 is its nonpolar {111} face, whereas its polar {001} face is the least stable, as indicated by the order of increasing surface energy density:

$$CeO_2\{111\}(0.69\,J\,m^{-2}) < CeO_2\{110\}(1.04\,J\,m^{-2}) < CeO_2\{001\}(1.41\,J\,m^{-2}). \qquad (26)$$

The formation energies (enthalpy changes) of O vacancies over each CeO_2 crystalline face were also evaluated by DFT calculations [77]:

$$CeO_2\{110\}(1.99\,eV) < CeO_2\{001\}(2.27\,eV) < CeO_2\{111\}(2.60\,eV). \qquad (27)$$

The order of the possibility of O vacancy formation (it is most likely on CeO_2\{110\}) in Eq. 27 correlates with the density of Cu^I sites if the CeO_2 is combined with Cu species. In the cases of nanospheres, nanorods, and nanocubes of CeO_2, stable {111}, relatively unstable {110} and unstable {001}, and unstable {001} faces were exposed, respectively [78–80]. DFT calculations revealed the order of the Cu^I site density on each nano-CeO_2:

$$\text{nanorod}(\{110\},\{001\}) > \text{nanocube}(\{001\}) > \text{nanosphere}(\{111\}), \qquad (28)$$

in accordance with the order in Eq. 27. In fact, CuO–CeO_2 nanorods exhibited higher CO conversion by a factor of 7.3 times compared to CuO–CeO_2 nanospheres in CO oxidation at 343 K (Table 4B, entries g and h) [78].

The activities of CO PROX were compared using CuO–CeO_2 catalysts based on CeO_2 nanospheres, nanorods, and nanocubes [79, 80]. The CO conversion decreased in the order

$$CuO-CeO_2 \text{ nanorods} > CuO-CeO_2 \text{ nanospheres} > CuO-CeO_2 \text{ nanocubes} \qquad (29)$$

at temperatures below 453 K (Table 4B, entries i–k), nearly in agreement with the trend in Eq. 28 [75].

The exchanges of multiple valence states of Cu and Ce in CuO–CeO_2 nanorods and their participation in CO PROX were investigated by XAFS, X-ray diffraction (XRD), and DRIFT under CO and O_2 [79]. At temperatures below 373 K, Cu^I species were easily formed under CO by the effects of CeO_2, as observed by DRIFT. At temperatures above 413 K, further reduction of Cu^I to Cu^0 was confirmed by XANES and XRD. The dispersed Cu^I and Cu^0 species were quickly reoxidized in O_2 at 393 K. The reduction of Cu^I to Cu^0 under CO was slower than the reduction of Cu^{II} to Cu^I under CO, whereas the reoxidation of Cu^I and Cu^0 to Cu^{II} was sufficiently fast not to be the rate-determining step. Thus, the $Cu^{II/0}$ redox process was inert toward CO oxidation, whereas the $Cu^{II/I}$ redox participated in the CO PROX cycle in consistent with reference 73.

However, the effects of Cu valence states are in controversy on CO PROX reactions. CO PROX tests were performed using CuO_x nanoparticles highly dispersed over CeO_2 nanorods prepared by a deposition–precipitation method [76]. An interatomic pair of Cu(–O–)Ce should be observed if the majority of Cu sites interact with Ce oxides to constitute a plausible interfacial active site for CO PROX. The peak was clearly observed in the Fourier transform of EXAFS spectra for CuO_x–CeO_2 nanorods in O_2 at 573 K. The peak negligibly varied under CO PROX temperatures as high as 473 K. Conversely, the peak disappeared if the sample was treated in H_2 at 573 K. Instead, an interatomic pair peak due to Cu–Cu emerged, indicating reduction of Cu^{II} to Cu^0 and deactivation of the catalyst. Unexpectedly, the activity and selectivity of the CO PROX reactions were improved by the H_2 pretreatment. Such Cu^0 sites were easily reoxidized to Cu^{II} under CO PROX reaction conditions; however, the peak due to the Cu(–O–)Ce pair never recovered. Therefore, highly-dispersed CuO_x species were suggested to be alternative active sites for CO PROX rather than Cu–O–Ce interface sites [76]. Ultimately, O vacancy at the interface between Cu and CeO_2 and that on the highly dispersed CuO_x may work similarly based on the formation energy of O vacancy (Eq. 26).

TPR and DRIFT studies revealed that the reducibility of CuO plays important roles in CO and H_2 oxidation processes. The Cu^I–CO sites near the boundary between CuO and CeO_2 were believed to be the active sites for CO oxidation, and the CuO sites reduced apart from CeO_2 were believed to act as H_2 oxidation sites; however, the wavenumber of Cu^I–CO rather than the amount correlated with the catalytic activity when CeO_2 nanorods, nanospheres, and nanocubes were used as supports for CuO. In the DRIFT spectra, the Cu^I–CO peak intensity for CuO–CeO_2 nanocubes was the strongest at 2115 cm^{-1} and 2099 cm^{-1} and the peaks were red-shifted. The red shift of the Cu^I–CO peak indicated that the CO on the CuO–CeO_2 nanocubes was thermally stable and that it was the cause of the lowest activity of this catalyst at lower temperatures among the three studied. By contrast, CuO–CeO_2 nanocubes exhibited the highest activity and selectivity at temperatures above 453 K. DFT calculations revealed that the adhesion energy of CuO over the preferred {001} face for CeO_2 nanocubes was 1.5 times greater than that over the {111} face. The strong interaction between CuO and the CeO_2 {001} face was suggested to maintain high CuO dispersion and to suppress formation of Cu^0, thus leading to the highest activity and selectivity at temperatures above 453 K.

In summary, the reaction mechanism over CuO–CeO_2 was proposed to include the redox of interface sites with CO and O_2 (Eq. 20), whereas H_2 oxidation was proposed to occur on metallic Cu sites. The correlations between the interface site number and the activity and also between the density of metal sites and the selectivity were confirmed based on kinetics, thermal analyses, and spectroscopic analyses. However, the dispersion of CuO and the nature of the CeO_2 surface were also critical to the CO PROX reaction. Well-dispersed CuO_x sites over CeO_2 nanorods were also reactive toward CO oxidation. Moreover, nanorod CeO_2 and {110} faces placed important roles in stabilizing CuO particles over CeO_2 and maintaining a good dispersion of CuO particles under CO PROX conditions.

3.2.3 *Cu-Based Catalysts Not Combined with CeO_2*

CuO–CeO_2 is among the most investigated noble-metal-free CO PROX catalysts; however, various Cu catalysts combined with reducible metal oxides other than CeO_2 have been also reported for CO PROX reactions. Importantly, reducibility of support materials for Cu is essential to reduce CO probably all via the Mars van Krevelen mechanism. Practically, to choose inexpensive reducible metal oxide is important rather than rare earth metal Ce oxide as the support of active Cu species.

As a general trend, Cu-based catalysts exhibit high activity utilizing the transformation between interfacial O atom and the vacancy (Scheme 4); however, the active temperature range (window) is relatively narrow and the selectivity is therefore not satisfactory primarily because the effective redox is between Cu^{2+} and Cu^{+}, but unfavorable Cu^{0} is formed at higher temperature that would proceed undesired by-reaction of H_2 oxidation. The $CuMn_2O_4$ catalyst is superior to CuO–CeO_2 based on the $T_{50\%}$ values at 427 and 454 K, respectively (Table 4B, entries m and n) [81]. Based on the standard reduction potential [1.71 V for Ce^{4+}/Ce^{3+} and 1.51 V for Mn^{3+}/Mn^{2+} vs. standard hydrogen electrode (SHE)], Ce^{4+} and Mn^{3+} are comparable for the reducibility of neighboring O site. $CuMn_2O_4$ is known as a mineral called Hopcalite that removes CO and/or N_2O from dry air; it is used in air filtration systems to purify breathing air for scuba diving and firefighting. The reaction mechanism has been proposed as involving the reaction of CO with oxidized metal ions and that of O_2 with reduced metal ions. It is proposed that the CO PROX reaction proceeds via the redox couples of Cu^{+}/Cu^{2+} and Mn^{3+}/Mn^{4+} as follows [81]:

$$CO + Cu^{2+} \rightarrow OC^{+}{-}Cu^{+}, \tag{30}$$

$$CO + Mn^{4+} \rightarrow OC^{+}{-}Mn^{3+}, \tag{31}$$

$$O_2 + Cu^{+} \rightarrow O_2^{-}{-}Cu^{2+}, \tag{32}$$

$$O_2 + Mn^{3+} \rightarrow O_2^{-}{-}Mn^{4+}, \tag{33}$$

and

$$\begin{aligned} &OC^{+}{-}(\text{reduced ion}) + O_2^{-}{-}(\text{oxidized ion}) \\ &\rightarrow O_2C{-}O{-}(\text{reduced ion}) + (\text{oxidized ion}) \\ &\rightarrow CO_2 + 2(\text{oxidized ion}), \end{aligned} \tag{34}$$

but the reaction cycle would be essentially similar to the Mars van Krevelen mechanism.

Cu–Mn oxides were tested for the CO PROX reaction, as inferred from the properties of Hopcalite [82]. CO conversion using Cu–Mn oxide (atomic ratio of Cu:Mn = 1:2) was 74 % at 373 K (Table 4B, entry o), which was lower than that achieved using Au/α-Fe_2O_3 (97–95 %; Table 4A, entries m and p) but was comparable to that achieved using CuO–CeO_2 (63–96 %; Table 4A, entries n and q) under similar reaction conditions (21–100 mL min^{-1}, 373 K). In fact, the $T_{50\%}$ values were of the same order as those of CO conversion:

$$\begin{aligned} &CuO{-}CeO_2(345{-}367\,K) \sim Cu{-}Mn(1{:}2)\,\text{oxide}\,(351\,K) \\ &> Au/\alpha - Fe_2O_3(310\,K). \end{aligned} \tag{35}$$

Cu-Fe-$K_{2x+y}Mn^{II}_{x}Mn^{III}_{y}Mn^{IV}_{8-x-y}O_{16}$ is based on the porous octahedral structure of $[Mn_8O_{16}]^{\delta-}$ [83]. Fe was included inadvertently, originating from the stainless steel balls used for ball-milling during the catalyst preparation. The CO PROX activity was higher than that of the Cu-free Fe-$K_{2x+y}Mn^{II}_{x}Mn^{III}_{y}Mn^{IV}_{8-x-y}O_{16}$ (Table 4B, entry s), suggesting that Cu–O–Mn bridging sites play an essential catalytic role, e.g., the redox between interface O and vacancy site (Scheme 4). The addition of CO_2 and/or moisture in the feed gas led to a decrease of the CO_2 conversion by a factor of 0.52–0.59 (Table 2j), mainly as a consequence of the blocking of CO adsorption sites and O vacancy sites for the CO PROX reaction. However, the CO_2 selectivity was not affected or was slightly improved by the addition of CO_2 and/or moisture, indicating that the reaction mechanism was not altered but the frequency was reduced (Table 2j). The WGSR (Eq. 1) and the reverse reaction ($H_2 + CO_2 \rightleftarrows H_2O + CO$) would affect the selectivity above a certain reaction temperature (~418 K).

Finally, CuO(17 wt%)–ZnO(46 wt%)–TiO_2(37 wt%) exhibited comparable CO PROX performances (CO conversion 32 % and PROX selectivity ~100 %) (Table 4B, entry t) to those using the other Cu catalysts in this section [84]. Similar to the other catalysts, in the presence of 15 % CO_2 in the reactant gas, the CO conversion decreased by a factor of 0.31, whereas the PROX selectivity remained constant at ~100 % (Table 2k). In this system, TiO_2 behaved as a reducible metal oxide support for CuO.

In summary, Cu catalysts, $CuMn_2O_4$, Cu–Mn (1:2) oxide, and Cu-Fe-$K_{2x+y}Mn^{II}_{x}Mn^{III}_{y}Mn^{IV}_{8-x-y}O_{16}$, exhibited activity for CO PROX reactions via the Mars van Krevelen mechanism similar to the activity of CuO–CeO_2 at flow rates of 50–600 mL min^{-1} and at 333–423 K because of the effects of reducible Mn^{3+} and/or Mn^{4+} at a comparable standard reduction potential to Ce^{4+}.

3.2.4 Co- and Ni-Based Catalysts

Co is known as a good catalyst for CO oxidation [85] and worthy to be tested for CO PROX as a substitute for Cu or noble metals. However, because CO methanation to consume H_2

$$CO + 3H_2 \rightarrow CH_4 + H_2O \tag{36}$$

would also proceed at 473 K using Co [86], CO PROX reactions using Co catalysts have been investigated at lower temperature than 473 K. The standard reduction potential for Co^{3+}/Co^{2+} is 1.92 V @SHE and would be advantageous compared to that for Cu^{2+}/Cu^{+} (0.159 V @SHE) if Co is included as Co^{3+} in the catalysts.

A Co–Mn (atomic ratio 8:1) oxide nanosheet catalyst was active (98 % conversion of CO) and selective (90 %) at 333 K (Table 4B, entry u) [87]. Under similar reaction conditions but at 348 K, a similar component Co–Mn–O–FeO_x achieved ~100 % conversion of CO (Table 4B, entry v) [88]. The $T_{50\%}$ values were less than 303 K for Co-Mn (8:1) oxide nanosheets and Co–Mn–O–FeO_x (Table 4B, entries t–v), suggesting excellent performance compared to noble-metal catalysts ($T_{50\%}$: 303–444 K) under similar reaction conditions (Table 4A, entries l–q). The Co_3O_4–$Ce_xZr_{1-x}O_2$ catalyst was also active; however, the $T_{50\%}$ value (383 K) was apparently higher than that for the Co–Mn oxide nanosheet or Co–Mn–O–FeO_x [89]. As the drawback, the poisoning effects of CO_2 addition and/or moisture addition were serious, especially with respect to CO conversion (~0–2.4 %, compared to 36 % when CO_2 and moisture were not included in the reactant using the Co_3O_4–$Ce_xZr_{1-x}O_2$ catalyst (Table 2l). A mixed spinel phase was found in the Mn-Co-Ce oxide, and it exhibited higher CO conversion (41 %) at 373 K compared to Mn–CeO_2 or Co–CeO_2 (Table 4B, entries x–z) [90]. The Mn–Co–Ce oxide was quite selective for CO PROX (~100 %) even in the presence of CO_2 (Table 2m). The mixed spinel phase enabled crystalline level of atomic dispersion of Co–O–Mn and Co–O–Ce rather than the mixing as the interface between nanoparticles and surface for supported catalysts.

Based on the same strategy as mixed spinel to maximize the metal–O–(another metal) connection as crystallines, Co and Cu ions were mixed in the octahedral molecular sieve (OMS) during the synthesis of OMS starting from $KMnO_4$ and $MnSO_4$ [91]. Their CO PROX activities and selectivities were quite high (Table 4B, entries α and β). Based on XPS and titration experiments performed on Mn ions, the formation of Co^{2+}–O^{2-}–Mn^{4+} bridging sites was proposed, in which $Co^{2+/+}$ and $Mn^{4+/3+}$ redox would oxidize O species and reduce O_2, respectively, and the charge would be transferred between the two metal ions. Furthermore, preliminary water tolerance was also demonstrated for Cu-OMS. The OMS crystalline structure may reduce the blocking effect of water.

Co_3O_4 has been supported on metal wire mesh [86]. Higher dispersion and higher conversion of CO PROX have been reported for the dispersion on metal wire mesh in comparison to Co_3O_4–SiO_2, Co_3O_4–Al_2O_3, Co_3O_4–TiO_2, Co_3O_4–ZrO_2, Co_3O_4–CeO_2, and Co_3O_4–$SrCO_3$. However, the low amount of catalyst charged (30 mg, Table 4B, entry γ) is likely the reason for the higher conversion. CoO_x–ZrO_2 was active at lower temperatures among the Co-based catalysts, and the $T_{50\%}$ values were 356–368 K (Table 4B, entries δ and ε) [92]. The CO conversion increased from 53 to 81 μmol h^{-1} g_{cat}^{-1} as the flow rate of reactant decreased from 50 to 25 mL min^{-1}, whereas the CO PROX selectivity did not change substantially (87–91 %). As most of the Co-catalysts in this paragraph are not supported on reducible oxides, Co–O–Co sites in well dispersed CoO_x may work as the CO oxidation sites similar to the proposed for CuO_x introduced in Sect. 3.2.2 [76]. Co–$SrCO_3$ exhibited poorer CO PROX activity, but the CO conversion reached 96 % at 513 K (Table 4B, entry ζ) [93]. The addition of CO_2 or both CO_2 and moisture reduced the CO conversion (to 38 and 27 %, respectively) compared to 96 % in the absence of CO_2 and moisture; however, the CO PROX selectivity did not substantially change (68–72 %; Table 2n). The addition of 0.3 mol % of Bi alleviated the negative effect of CO_2 and moisture (63 % CO conversion; Table 2o).

In comparison to Cu and Co, Ni was coupled with Fe oxide as $NiFe_2O_4$; however, it was inactive even at 473 K (CO conversion 9.1 %, Table 4B, entry η) [94]. Although Ni surface sometimes behaves similar to Co or Cu surface in heterogeneous catalysis, Ni^{2+} is difficult to be one-electron reduced and the standard reduction potential for Ni^{2+}/Ni^{0} is quite negative: −0.257 V @SHE and would not accept electron from neighboring O atom to make O vacancy (Scheme 4).

In summary, when Co was combined with reducible metal oxides, e.g., Mn, Fe, and Ce oxides or ZrO_2, the CO PROX conversion was 2–100 % with a selectivity of 81–100 % at reactant flow rates between 25 mL min^{-1} and 250 mL min^{-1} at 333–373 K. These results demonstrate that Co exhibits CO PROX activity similar to that of Cu in the expectation of practical application of CO PROX. Co^{3+} would be favorable similar to Cu^{2+} based on the standard reduction potential for oxidation capacity, however Ni^{2+} should be disadvantageous.

3.2.5 Binary Metal–Organic Framework (MOF) Catalysts

Based on Sects. 3.2.1, 3.2.2, 3.2.3, 3.2.4, Cu or Co combined with reducible metal oxides were excellent for CO PROX, and more importantly in the practical point of view, mixed spinel or OMS crystalline structure seemed advantageous to inhibit the blocking effect of CO_2 [90] or moisture [91]. In this context, MOFs are widely investigated in chemical applications, and one of the most widely explored area of applications is catalysis, e.g., acid/base catalysis [95, 96], organic reactions [97, 98], organic reactions catalyzed by metals (Pd, Au, Ru, Cu, Pt, Ni, and Ag) embedded in MOFs [98, 99], asymmetric catalysis [96, 100, 101], CO oxidation [98], photocatalysis [98], and hydrodesulfurization [98]. CO PROX tests conducted under the conditions of CO 0.51 kPa, O_2 0.51 kPa, H_2 50.1 kPa, and balance N_2 gas and 100 mg of catalyst using a flow reaction system at 323 K (Fig. 9) in the presence of "binary MOF" catalysts synthesized from general MOF crystallites with second metal salts (Scheme 5) in the expectations of effective Cu–O–Ti connection and to mitigate the blocking effect of CO_2 and/or moisture [102].

MOFs are advantageous in comparison to classic bulk materials in the applications of sorption and catalysis because of their high surface areas, which result from their porous structures (Scheme 5a, b), e.g., $[Ti_8O_8(OH)_4]^{12+}$ clusters are interlinked by organic ligands (terephthalates) to form a porous crystal structure (MIL125) [103]. Apparently, $[Ti_8O_8(OH)_4]^{12+}$ clusters in MIL125 are more dispersed than any type of TiO_2 bulk material. Secondary metal Cu oxyhydroxide linkers can replace some of the organic linkers (yellow/thinner connectors in Scheme 5) in binary MOFs (Scheme 5c). Binary MOFs are a crystal model of supported catalysts (Scheme 5a) because the interface between the primary metal ion/cluster and secondary metal represents the ultimate dispersion of interface sites of classic supported catalysts.

With the binary MOF Cu-MIL125, which was synthesized from MIL125 and Cu nitrate aqueous solution with a Cu/Ti atomic ratio of 1/2 and heated at 613 K, the CO PROX rate stabilized at 3 h from the start of reaction (Fig. 9A1), and the conversion to CO_2 stabilized at 67–76 % at 3–24 h (Fig. 9A2 and Table 4B, entry ι). Water was detected until 4 h from the start of the reaction, but disappeared at 4–24 h (Fig. 9A1). Accordingly, the CO PROX selectivity was 98–99 % at 4–24 h (Fig. 9A2 and Table 4B, entry ι), consistent with the 98 % selectivity reported for the same catalyst at a lower pressure of 6.5 kPa (Table 4B, entry μ) [102]. When the CO PROX tests were repeated without contact with air, the initial water formation was negligible. This result suggests that the water detected between 0 h and 4 h in Fig. 9A1 exclusively desorbed from the catalyst and was not a catalytic product derived from O_2 reduction by H_2.

In comparison, in the case of $CuO–CeO_2$ as the catalyst, the CO oxidation rate increased proportionally until 4 h from the start of the test and gradually increased for 24 h (Fig. 9B1). Correspondingly, the conversion to CO_2 gradually increased from 16 % at 4 h to 28 % at 24 h (Fig. 9B2; Table 4B, entry θ). Conversely, the CO PROX selectivity stabilized at 93–96 % at 4–24 h (Fig. 9B2; Table 4B, entry θ), consistent with the 90 % selectivity obtained in the lower-pressure test of the same catalyst at 6.5 kPa (Table 4B, entry λ) [93].

In summary, under the reaction conditions listed in Fig. 9, the conversion to CO_2 using the binary MOF Cu-MIL125 was higher by a factor of 4.3–2.7 than the conversion obtained using $CuO–CeO_2$ under the same conditions, demonstrating the practical importance of the binary

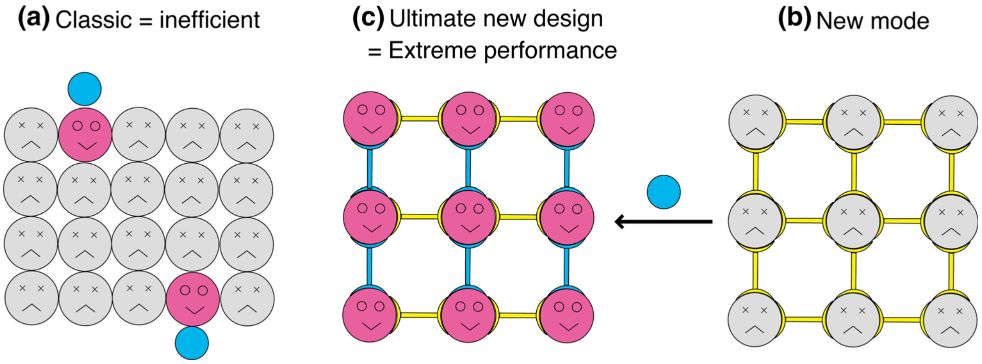

Scheme 5 Binary MOF concept. **a** Traditional metal/metal oxide supported catalysts in which support in contact with metal/metal oxide (*blue/darker spheres*) is active (*red/darker faces*); **b** general MOF in which metal ions or metal oxyhydroxy clusters (*gray/thinner faces*) are linked by organics (*yellow/thinner connectors*); and **c** new design of binary MOF in which metal ions or metal oxyhydroxy clusters (*red/darker faces*) are linked by both organics (*yellow/thinner connectors*) and second metal hydroxides (*blue/darker connectors*) (Color figure online)

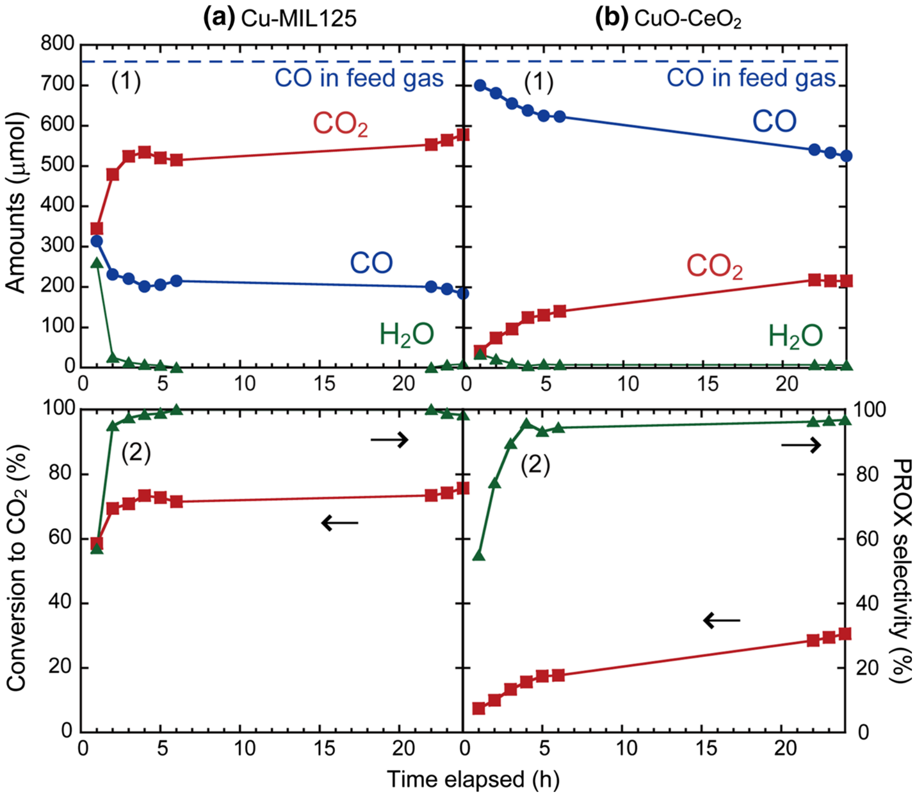

Fig. 9 Time courses of PROX tests in CO (0.5 %) + O_2 (0.5 %) + H_2 (49.5 %) + N_2 (49.5 %) at flow rate of 20 mL min^{-1} using **a** Cu-MIL125 and **b** CuO–CeO_2. Catalyst amount 100 mg, temperature 323 K. *1* Amounts of CO_2, CO, and H_2O in exit gas sampled (40 mL) and *2* conversion to CO_2 = 100 × $[CO_2]_{exit\ gas}/[CO]_{feed\ gas}$ (*filled square*) and CO PROX selectivity = 100 × $[CO_2]_{exit\ gas}/([CO_2]_{exit\ gas} + [H_2O]_{exit\ gas})$ (*filled triangle*) [102]. Copyright (2015) Elsevier

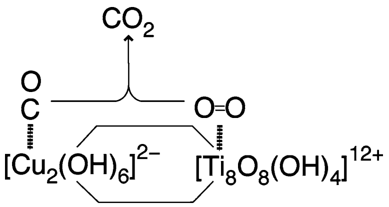

Scheme 6 Proposed reaction sites for CO PROX reaction using Cu-MIL125-I catalysts [102]. Copyright (2015) Elsevier

metal (Ti, Cu) MIL125-derived catalyst. This is a crystal model of Cu catalyst with reducible metal oxide to adsorb CO and O_2, respectively (Scheme 6). The binary MOF is hopeful, however, it needs further development to alleviate the blocking effect of CO_2 and/or moisture [102].

4 Concluding Remarks

In the photocatalytic CO PROX reactions in predominant H_2, CO conversions of 89–100 % were achieved using molecular (metal complex-like) photocatalysts (Mo–SiO_2 and Cr–MCM-41) and semiconductor photocatalysts (NiO/TiO_2 and Cu–ZnO) under UV and/or visible light, with high PROX selectivity (97–99 %). These photocatalysts do not activate H_2 via polar bond dissociation mechanism whereas H_2 is easily activated over noble metal full of free electrons especially at higher temperatures than 473 K leading to lower selectivity of CO PROX reactions. CO and O_2 reacted at the active site (Mo=O) over Mo–SiO_2 activated by the charge separation at the bond due to the absorption of photons. Photo-PROX was initiated by the charge separation also for Cu–ZnO. However, O_2 was reduced on photoreduced Cu sites over ZnO{ $10\bar{1}1$ } rather than on the interface sites; CO adsorbed onto ZnO($000\bar{1}$) to form formate species combined with hydroxy groups and was photooxidized to CO_2. When irradiated by UV or visible light, PROX reaction rates using typical thermal PROX catalysts (Au/TiO_2 and Au–CuO/TiO_2) increased by a factor of 1.03–3.2 due to the SPR effect of Au and charge separation in TiO_2 and the subsequent electron transfer from TiO_2 to Au.

The CO PROX mechanism using CuO–CeO_2 is considered to proceed via the Mars van Krevelen mechanism, in which CO reacts with lattice O at the interface between CuO and CeO_2 and then forms an O vacancy that is subsequently recovered by O_2. Cu was also effective when it was supported on reducible metal oxides other than CeO_2. $CuMn_2O_4$, Cu–Mn (1:2) oxide, and $Cu\text{-}Fe\text{-}K_{2x+y\text{-}}Mn_x^{II}Mn_y^{III}Mn_{8-x-y}^{IV}O_{16}$ exhibited comparable activities for CO PROX reactions to $CuO–CeO_2$ at flow rates of 50–600 mL min^{-1} and at 333–423 K because of the effects of reducible Mn. The CO PROX activity of Cu or Co on reducible metal oxides would be rationalized based on the standard reduction potential for Cu^{2+}, Co^{3+}, Ce^{4+}, and $Mn^{3+/4+}$.

Modeling and extraction of active sites of classical $CuO–TiO_2$ for CO PROX were enabled using MOF (MIL125) as a Ti oxyhydroxide precursor reacted with Cu hydroxides. The CO PROX conversion achieved using the binary MOF at 323 K was 4.3 times higher than that achieved using $CuO–CeO_2$. For the fuels in a worldwide H_2 society unlimited by expensive elements, metal complex-like and semiconductor-based photocatalysts and thermal catalysts consisting of Cu or Co and reducible metal oxides are especially promising for small-scale/personal H_2 purification. However, further progress is needed to alleviate the activity loss of CO PROX in the presence of moisture and/or CO_2. Microporous crystallines, e.g., mixed spinel, OMS, and MOF, are also expected to exhibit steric hindrance to suppress the blocking of moisture and/or CO_2.

Acknowledgments The authors are grateful for the financial support from the Grant-in-Aid for Scientific Research C (26410204, 22550117) and Research Fellowship for Young Scientists (25·489; Y.Y.) from the Japan Society for the Promotion of Science and for approval of the Photon Factory Proposal Review Committee for X-ray measurements (2014G631, 2013G159, 2011G083, 2009G552, 2009G596) and the Priority Program for Disaster-Affected Quantum Beam Facilities (2011A1978, SPring-8 & KEK). The authors would like to thank Enago (www.enago.jp) for the English language review.

References

1. Schlapbach L (2009) Nature 460:809–811
2. Kraytsberg A, Ein-Eli Y (2014) Energy Fuels 28:7303–7330
3. Izumi Y (2013) Coord Chem Rev 257:171–186
4. Gasteiger HA, Marković NM (2009) Science 324:48–49
5. Rouquerol F, Rouquerol J, Sing K (1999) Adsorption by powders and porous solids—principles, methodology, and applications. Academic Press, London, pp 357–358
6. Lin YM, Rei MH (2001) Sep Purif Technol 25:87–95
7. Cho A (2003) Science 299:1684–1685
8. Park ED, Lee D, Lee HC (2009) Catal Today 139:280–290
9. Bion N, Epron F, Moreno M, Mariño F, Duprez D (2008) Top Catal 51:76–88
10. Lakshmanan P, Park JE, Park ED (2014) Catal Surv Asia 18:75–88
11. Beckers J, Rothenberg G (2010) Green Chem 12:939–948
12. Kudo A, Miseki Y (2009) Chem Soc Rev 38:253–278
13. Izumi Y (2015) Recent advances (2012–2015) in the photocatalytic conversion of carbon dioxide to fuels using solar energy: feasibility for a new energy. In: Jin F, He LN, Hu YH (eds) ACS books advances in CO_2 capture, sequestration, and conversion, vol 1194, pp 1–46
14. Yoshida Y, Mitani Y, Itoi T, Izumi Y (2012) J Catal 287:190–202
15. Sato S, White JM (1980) J Am Chem Soc 102:7206–7210
16. Linsebigler A, Lu G, Yates JT Jr (1996) J Phys Chem 100:6631–6636
17. Rosseler O, Ulhaq-Bouillet C, Bonnefont A, Pronkin S, Savinova E, Louvet A, Keller V, Keller N (2015) Appl Catal B 166(167):381–392
18. Hoffmann MR, Martin ST, Choi W, Bahnemann DW (1995) Chem Rev 95:69–96
19. Kamegawa T, Takeuchi R, Matsuoka M, Anpo M (2006) Catal Today 111:248–253
20. Banker G (2010) Introduction to XAFS. Cambridge University Press, Cambridge
21. Matsuoka M, Kamegawa T, Takeuchi R, Anpo M (2007) Catal Today 122:39–45
22. Zhang Y-Z, Zhou B, Zhang X-P, Huang P, Li C-H, Liu Y (2009) J Hazard Mater 163:1345–1352
23. Di Marco G, Lanza M, Mamo A, Stefio I, Pietro CD, Romeo G, Campagna S (1998) Anal Chem 70:5019–5023
24. Matsuoka M, Kamegawa T, Anpo M (2007) Stud Surf Sci Catal 165:725–728
25. Kamegawa T, Morishima J, Matsuoka M, Thomas JM, Anpo M (2007) J Phys Chem C 111:1076–1078
26. Anpo M, Kim T-H, Matsuoka M (2009) Catal Today 142:114–124
27. Kamegawa T, Kim TH, Morishima J, Matsuoka M, Anpo M (2009) Catal Lett 129:7–11
28. Yoshida Y, Itoi T, Izumi Y (2015) J Phys Chem C 119:21585–21598
29. Chen X, Mao SS (2007) Chem Rev 107:2891–2959
30. Izumi Y, Itoi T, Peng S, Oka K, Shibata Y (2009) J Phys Chem C 113:6706–6718
31. Izumi Y, Shibata Y (2009) Chem Lett 38:912–913
32. Izumi Y, Konishi K, Obaid D, Miyajima T, Yoshitake H (2007) Anal Chem 79:6933–6940
33. Izumi Y, Kiyotaki F, Yagi N, Vlaicu AM, Nisawa A, Fukushima S, Yoshitake H, Iwasawa Y (2005) J Phys Chem B 109:14884–14891
34. Masih D, Yoshitake H, Izumi Y (2007) Appl Catal A 325:276–282
35. Pickering IJ, George GN (1995) Inorg Chem 34:3142–3152
36. Solomon EI, Jones PM, May JA (1993) Chem Rev 93:2623–2644
37. Izumi Y, Oyanagi H, Nagamori H (2000) Bull Chem Soc Jpn 73:2017–2023
38. Izumi Y, Nagamori H (2000) Bull Chem Soc Jpn 73:1581–1587
39. Izumi Y, Nagamori H, Kiyotaki F, Masih D, Minato T, Roisin E, Candy J-P, Tanida H, Uruga T (2005) Anal Chem 77:6969–6975
40. Kau LS, Spira-Solomon J, Penner-Hahn JE, Hodgson KO, Solomon EI (1987) J Am Chem Soc 109:6433–6442
41. Kawamura S, Puscasu MC, Yoshida Y, Izumi Y (2015) Appl Catal A 504:238–247
42. Morikawa M, Ahmed N, Yoshida Y, Izumi Y (2014) Appl Catal B 144:561–569
43. Kawamura S, Ahmed N, Carja G, Izumi Y (2015) Oil Gas Sci Technol 70:841–852
44. Youn SK, Ramgir N, Wang C, Subannajui K, Cimalla V, Zacharias M (2010) J Phys Chem C 114:10092–10100
45. Di L, Wu G, Dai W, Guan N, Li L (2015) Fuel 143:318–326
46. Niu T, Shen LM, Liu Y (2013) Porous Mater 20:789–798
47. Niu T, Zhang LH, Liu Y (2014) Int J Hydrog Energy 39:13800–13807
48. Niu T, Liu GL, Liu Y (2014) Appl Catal B 154(155):82–92

49. Haruta M, Yamada N, Kobayashi T, Iijima S (1989) J Catal 115:301–309
50. Sanchez A, Abbet S, Heiz U, Schneider WD, Hakkinen H, Barnett RN, Landman U (1999) J Phys Chem A 103:9573–9578
51. Bamwenda GR, Tsubota S, Nakamura T, Haruta M (1997) Catal Lett 44:83–87
52. Green IX, Tang W, Neurock M, Yates JT Jr (2011) Science 333:736–739
53. Saavedra J, Doan HA, Pursell CJ, Grabow LC, Chandler BD (2014) Science 345:1599–1602
54. Izumi Y, Obaid D, Konishi K, Masih D, Takagaki M, Terada Y, Tanida H, Uruga T (2008) Inorg Chim Acta 361:1149–1156
55. Herzing AA, Kiely CJ, Carley AF, Landon P, Hutchings GJ (2008) Science 321:1331–1335
56. Singh JA, Overbury SH, Dudney NJ, Li M, Veith GM (2012) ACS Catal 2:1138–1146
57. Ketchie WC, Murayama M, Davis RJ (2007) Top Catal 44:307–317
58. Ojeda M, Zhan B-Z, Iglesia E (2012) J Catal 285:92–102
59. Lippard SJ, Berg JM (1994) Principle of bioinorganic chemistry. University Science Books, Mill Valley, pp 55–56
60. Avgouropoulos G, Ioannides T, Papadopoulou CH, Batista J, Hocevar S, Matralis HK (2002) Catal Today 75:157–167
61. White JL, Baruch MF, Pander JE III, Hu Y, Fortmeyer IC, Park JE, Zhang T, Liao K, Gu J, Yan Y, Shaw TW, Abelev E, Bocarsly AB (2015) Chem Rev 115:12888–12935
62. Ahmed N, Shibata Y, Taniguchi T, Izumi Y (2011) J Catal 279:123–135
63. Dai W, Zheng X, Yang H, Chen X, Wang X, Liu P, Fu X (2009) J Power Sources 188:507–524
64. Clavero C (2014) Nat Photonics 8:95–103
65. Yang K, Li Y, Huang K, Chen X, Fu X, Dai W (2014) Int J Hydrog Energy 39:18312–18325
66. Yang K, Huang K, Lin L, Chen X, Dai W, Fu X (2015) J Power Sources 284:194–205
67. Yang K, Liu J, Si R, Chen X, Dai W, Fu X (2014) J Catal 217:229–239
68. Mariño F, Descorme C, Duprez D (2005) Appl Catal B 58:175–183
69. Lu J-Q, Sun C-X, Li N, Jia A-P, Luo M-F (2013) Appl Surf Sci 287:124–134
70. Polster CS, Nair H, Baertsch CD (2009) J Catal 266:308–319
71. Lee HC, Kim DH (2008) Catal Today 132:109–116
72. Sun S, Mao D, Yu J, Yang Z, Lu G, Ma Z (2015) Catal Sci Technol 5:3166–3181
73. Martínez-Arias A, Gamarra D, Fernández-García M, Hornés A, Bera P, Koppány Z, Schay Z (2009) Catal Today 143:211–217
74. Caputo T, Lisi L, Pirone R, Russo G (2008) Appl Catal A 348:42–53
75. Yao S, Mudiyanselage K, Xu W, Johnston-Peck AC, Hanson JC, Wu T, Stacchiola D, Rodriguez JA, Zhao H, Beyer KA, Chapman KW, Chupas PJ, Martínez-Aries A, Si R, Bolin TB, Liu W, Senanayake SD (2014) ACS Catal 4:1650–1661
76. Wang W-W, Du P-P, Zou S-H, He H-Y, Wang R-X, Jin Z, Shi S, Huang Y-Y, Si R, Song Q-S, Jia C-J, Yan C-H (2015) ACS Catal 5:2088–2099
77. Nolan M, Parker SC, Watson GW (2005) Surf Sci 595:223–232
78. Zhou K, Xu R, Sun X, Chen H, Tian Q, Shen D, Li Y (2005) Catal Lett 101:169–173
79. Gamarra D, Cámara AL, Monte M, Rasmussen SB, Chinchilla LE, Hungría AB, Munuera G, Gyoriffy N, Schay Z, Corberán VC, Conesa JC, Martínez-Arias A (2013) Appl Catal B 130(131):224–238
80. Monte M, Gamarra D, Cámara AL, Rasmussen SB, Gyoriffy N, Schay Z, Martínez-Arias A, Conesa JC (2014) Catal Today 229:104–113
81. Valdés-Solís T, López I, Marbán G (2010) Int J Hydrog Energy 35:1879–1887
82. Hasegawa Y, Maki R, Sano M, Miyake T (2009) Appl Catal A 371:67–72
83. Hernández WY, Centeno MA, Ivanova S, Eloy P, Gaigneaux EM, Odriozola JA (2012) Appl Catal B 123(124):27–35
84. Moretti E, Storaro L, Talon A, Patrono P, Pinzari F, Montanari T, Ramis G, Lenarda M (2008) Appl Catal A 344:165–174
85. Xie X, Li Y, Liu Z-Q, Haruta M, Shen W (2009) Nature 458:746–749
86. Marbán G, López I, Valdés-Solís T, Fuertes AB (2008) Int J Hydrog Energy 33:6687–6695
87. Zhao Z, Lin J, Wang G, Muhammad T (2015) AIChE J 61:239–252
88. Zhao Z, Li Y, Bao T, Wang G, Muhammad T (2014) Catal Commun 46:28–31
89. Zhao Z, Jin R, Bao T, Lin X, Wang G (2011) Appl Catal B 110:154–163
90. Gómez LE, Miró EE, Boix AV (2013) Int J Hydrog Energy 38:5645–5654
91. Xia GG, Yin YG, Willis WS, Wang JY, Suib SL (1999) J Catal 185:91–105
92. Yung MM, Zhao Z, Woods MP, Ozkan US (2008) J Mol Catal A 279:1–9
93. Omata K, Kobayashi Y, Yamada Y (2007) Catal Commun 8:1–5
94. Santos PTA, Costa ACFM, Kiminami RHGA, Andrade HMC, Lira HL, Gama L (2009) J Alloys Compd 483:399–401
95. Bhattacharjee S, Lee Y-R, Puthiaraj P, Cho S-M, Ahn W-S (2015) Catal Surv Asia 19:203–222
96. Farrusseng D, Aguado S, Pinel C (2009) Angew Chem 48:7502–7513
97. Liu J, Chen L, Cui H, Zhang J, Zhang L, Su C-Y (2014) Chem Soc Rev 43:6011–6061
98. Corma A, García H, Llabrés i Xamena FX (2010) Chem Rev 110:4606–4655
99. Dhakshinamoorthy A, Garcia H (2012) Chem Soc Rev 41:5262–5284
100. Yoon M, Srirambalaji R, Kim K (2012) Chem Rev 112:1196–1231
101. Ma L, Abney C, Lin W (2009) Chem Soc Rev 38:1248–1256
102. Yoshida Y, Izumi Y (2015) J Catal 332:1–12
103. Dan-Hardi M, Serre C, Frot T, Rozes L, Maurin G, Sanchez C, Férey G (2009) J Am Chem Soc 131:10857–10859